Chapter 2: Multiscale Modeling of Tensile Failure in Fiber-Reinforced Composites

Zhenhai Xia[1] and W.A. Curtin[2]

[1]Department of Mechanical Engineering, The University of Akron, Akron, OH 44325, USA
[2]Division of Engineering, Brown University, Providence, RI 02912, USA

2.1 Multiscale Damage and Failure of Fiber-Reinforced Composites

Fiber-reinforced composites can be engineered to exhibit high strength, high stiffness, and high toughness, and are, thus, attractive alternatives to monolithic polymer, metals, and ceramics in structural applications. To engineer the material for high performance, the relationship between material microstructure and its properties must be established to accurately predict the deformation and failure. Such a relationship between underlying constituent material properties and composite performance can also aid selection and/or optimization of new composite systems. Successful models can yield predictive insight into the origins of damage tolerance, size scaling, and reliability of existing composite systems and can be extended to investigate damage and failure under more complex loading and environmental conditions, such as fatigue and stress rupture.

Damage relevant to macroscopic failure of fiber-reinforced composite occurs at many length scales and by a variety of physical mechanisms. At the smallest scale, preexisting defects in the fibers propagate and form fiber cracks that impinge on the matrix and the interface. Debonding, sliding, and/or matrix yielding at the crack perimeter inhibit crack propagation into the matrix; but the ensuing deformations are complex. The load carried by the broken fiber is then redistributed among the remaining unbroken fibers and matrix as determined by the detailed conditions at the debonded fiber/matrix interface and in the matrix. Subsequent damage occurs in and around other fibers according to the statistical distribution of flaws in the fibers and the stresses acting on those flaws due to the applied stress and the stress redistribution. Eventually, macrocracks will form and grow, leading to failure of the composites. Figure 2.1 illustrates the damage evolution of fiber-reinforced composites at each length scale under different loading conditions.

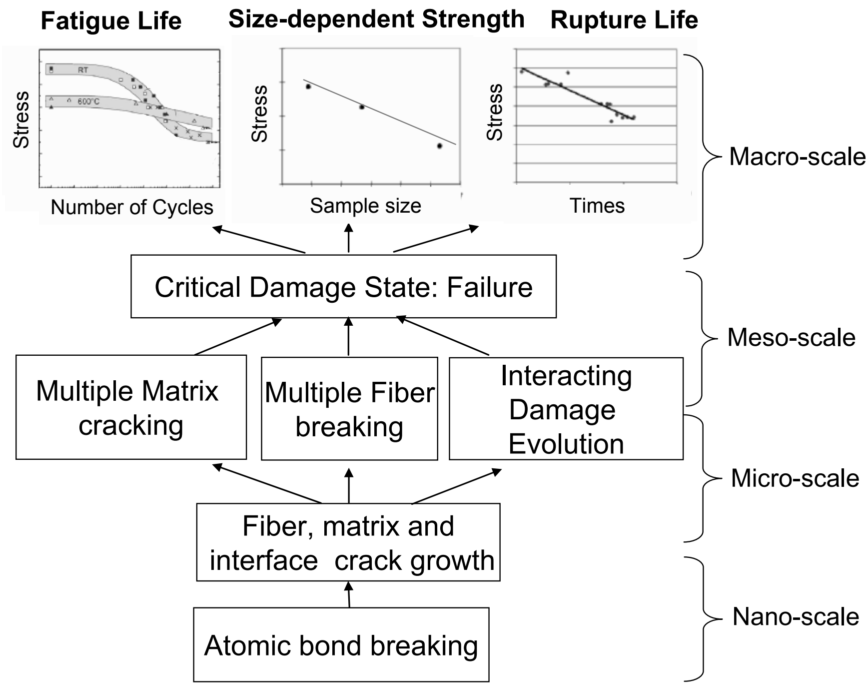

Fig. 2.1. Multiscale damage and failure in fiber-reinforced composites

Although the modeling path is conceptually clear, direct simulation of composite materials is still not a viable option despite advances in computational techniques and computing power. Finite element models that can capture micromechanical effects of cracks at the fiber/matrix/interface scale generally must employ mesh sizes of the order of the size of the microstructure and can result in an algebraic system with many millions of unknowns. It is insufficient, however, to focus only on one scale, i.e., a fiber break and the myriad details associated with it. On the other hand, homogenization and averaging techniques for analyzing heterogeneous materials, while possibly leading to manageable problem sizes, do not provide information about the microscopic fields needed, for example, to predict failure. Thus, there is a need for accurate and computationally efficient techniques that take into account the most important scales involved in the goal of the simulation while permitting the analyst to choose the level of accuracy and detail of description desired. Therefore, a *multiscale modeling* strategy is needed to accurately handle the evolution of damage at the larger scales while retaining important small-scale details and, thus, to accurately predict mechanical properties and performance of fiber-reinforced composites.

There are two main multiscale modeling techniques for materials: seamless coupling of methods in a single computational framework and hierarchical information transfer. Direct coupling methods are not viable for fiber composite problems because the damage spans a range of scales, and it is not possible to focus on one microscopic region in detail surrounded by a less-detailed description. Thus, the hierarchical multiscale modeling approach, in which the information of simulations at small length scales is processed and fed into larger-scale models, is preferable. The need for multiscale analyses has been well recognized; but until recently there has not been a direct connection made between the detailed structures at the fiber/matrix/interface scale, the multifiber damage problem, and large-scale component performance. Most work has assumed some approximate representation of the behavior at the smallest scale and pursued the larger-scale damage evolution. Such approaches are certainly warranted for understanding broad trends, identifying characteristic length scales associated with the damage, and for guiding the development of analytic models [5, 21, 31]. Other work has investigated the detailed stress states around damaged fibers, matrix, and/or interfaces but then employed only very simple models of overall composite behavior to indicate the important role of the microscale damage [12]. Specific system design and optimization requires attention to the detailed micromechanics of damage and load transfer around individual fiber breaks and the inclusion of such information directly into accurate larger-scale models.

In this chapter, one multiscale modeling approach for predicting tensile strengths of unidirectional fiber composites, including metal, polymer, and ceramic matrix composites will be reviewed. The quantitative success of this approach in predicting the tensile strength and its size dependence in a carbon fiber-reinforced plastic (CFRP), silicon carbide fiber/titanium matrix composites (TMCs), and alumina fiber/aluminum matrix composite (AMC) will be demonstrated. Finally, the approach will be extended to the prediction of strength and low-cycle fatigue life of TMCs.

This review emphasizes the published work of the present authors on multiscale modeling and simulation cast into a single overall framework. Progress in the field at one or several coupled scales has been made by many workers, with important insights and advances. In addition, analytic models for many problems in composite failure have been devised, but those works are not discussed here. Hence, the work presented here is not a comprehensive review of the literature. Interested readers can refer to several previous significant review articles [7, 22, 27] as well as other papers [19].

2.2 Multiscale Modeling via Information Transfer

2.2.1 Model Description and General Strategy

The fiber-reinforced composites considered here consist of continuous cylindrical fibers embedded in a matrix material in a unidirectional (aligned) arrangement. Such a composite can also be considered as a ply, a basic unit of a laminated composite structure. To develop a relationship between macroscopic properties and microstructure of the composite, a hierarchical set of models addressing physical phenomena at successive larger lengths scale, with coupling through information transfer, is introduced, as illustrated in Fig. 2.2. Figure 2.2 shows the full possible range of studies relevant to the problem. At the smallest scales, an atomistic or quantum analysis can assess features such as interface fracture energy and crack deflection at the bimaterial fiber/matrix interface. Key information on interfacial debonding and sliding is then passed into a continuum interface model, e.g., a cohesive zone, used in a micromechanical unit cell model consisting of matrix and a number of fibers to compute the stress redistribution around a fiber break for a particular material system. The stress redistribution is condensed into stress concentration factors on unbroken fibers, and, perhaps, stress intensity factors on matrix cracks, and this information is transferred to a larger-scale Monte Carlo model that tracks the evolution of fiber and/or matrix damage with increasing applied load. Details of the deformation around each fiber break are not retained at this scale, only their effects on stress concentrations. The Monte Carlo model is used to simulate damage up to the point of tensile failure, leading to a predicted average strength and statistical distribution for a composite sample that is small on the scale of practical samples but large compared to the critical damage size that drives failure. The tensile strength distribution calculated from the Monte Carlo model is then employed in analytic weak-link size-scaling models to predict ply strength and its statistical distribution as a function of physical size. Finally, the ply strength is used in standard laminated composite models to predict the strength and reliability of the composite component. In the last stage, other damage phenomena such as interply delamination can occur and change the local stresses in the plies themselves. In such cases, the ply strength vs. size can be used at smaller scales to assess the onset of local ply damage due to these other damage modes.

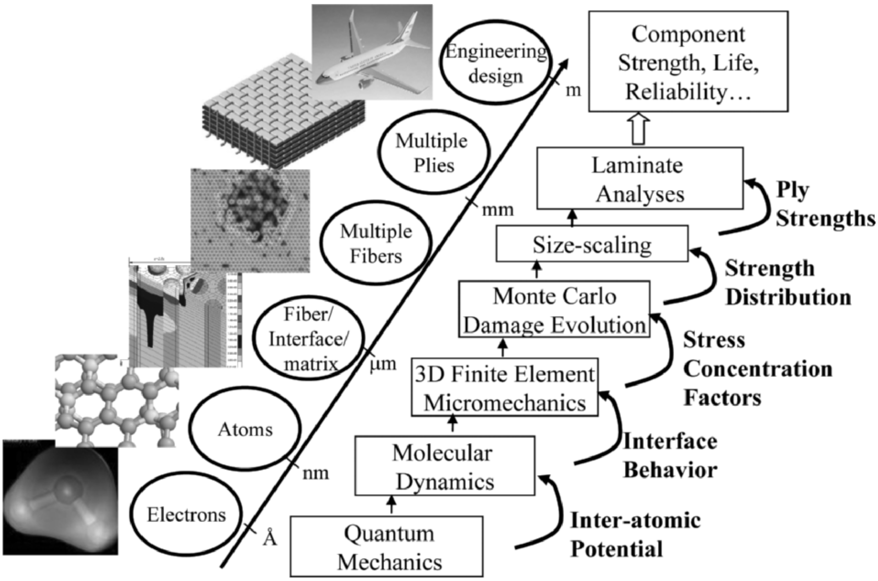

Fig. 2.2. Approach to multiscale modeling: scale coupling via information transfer

It is not necessary to always start from the quantum mechanical scale and progress upward. In fact, the goal of composite design is to shift the critical scale of damage from the nanoscale, e.g., the crack tip, to the much larger, observable, and detectable scale of collective fiber damage. Since a single fiber break does not initiate macroscopic failure, the details of the behavior at the smaller scales, while important, are not sufficient to predict failure. Therefore, one strategy is to envision possible modes of interface debonding and fiber/matrix constitutive behavior, as motivated by experiments or other theoretical models, and then use the multiscale modeling approach starting at the micromechanical scale. Parametric studies of the effect of interface and matrix behavior on the macroscopic fracture can then point to issues at smaller scales that would merit more detailed treatment. The work presented in this chapter focuses on the multiscale modeling of unidirectional fiber-reinforced composites starting from the micromechanical scale taking the interface behavior as a parametric input with quantities such as the interfacial coefficient of friction and interfacial strength obtained from experiments when applications to a particular material system are made.

2.2.2 Micromechanics at the Fiber/Matrix/Interface Scale

The goal of modeling at the micromechanics scale is to compute the detailed stress redistribution around broken fibers with various interfacial deformation models and extract from such studies the average stress concentrations induced in the surrounding unbroken fibers and the stress recovery along the broken fiber due to interface shear resistance. Since introduction of a fiber break or a matrix crack causes large stress changes only in the vicinity of the crack, a small-scale model with high spatial refinement is used. The model used consists of a hexagonal array of unidirectional fibers with a fiber volume fraction of V_f. Making use of symmetry, the model can be restricted to a 30° wedge, as shown in Fig. 2.3a. Each fiber in this wedge section represents a distinct set of neighbors relative to the central fiber. A 3D finite element representation of this model is then constructed to calculate the stress distributions around broken fibers (Fig. 2.3b,c). The axial length of the model depends on the interface and matrix behavior and is generally chosen such that the stress distribution at the end of the model is not affected by the stress redistributions caused by the introduction of fiber or matrix damage at the midplane. The size of the model in the radial direction (perpendicular to the fibers) is chosen so that the deformation of fibers at the outer perimeter is not affected by the imposed fiber damage. For example, with a single central broken fiber, we use the nearest eight sets of neighbors (43 fibers total). With seven broken fibers (fibers 1 and 2 broken in the 30° wedge section), a larger model extending out to tenth neighbors and containing a total of 91 fibers is used. The mesh sizes are selected to obtain converged results, for which there is no a priori guidance except that there should be at least several elements in the matrix region between the fibers and within the fibers themselves. The model is subjected to tensile loading along the axis of the fibers, and the appropriate boundary conditions are shown in Fig. 2.3b. The nodes of uncracked material at the crack plane ($z = 0$) have fixed displacements in the z-direction while the outer surface of the model is traction free.

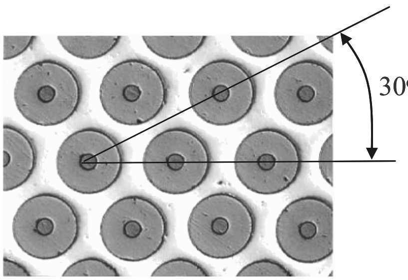

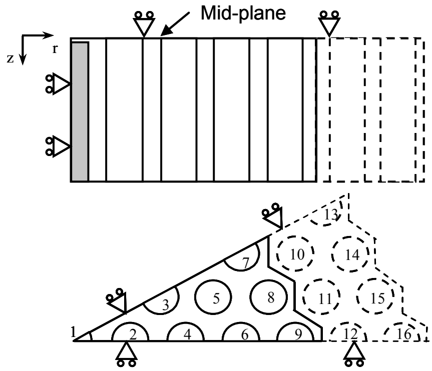

(a) (b)

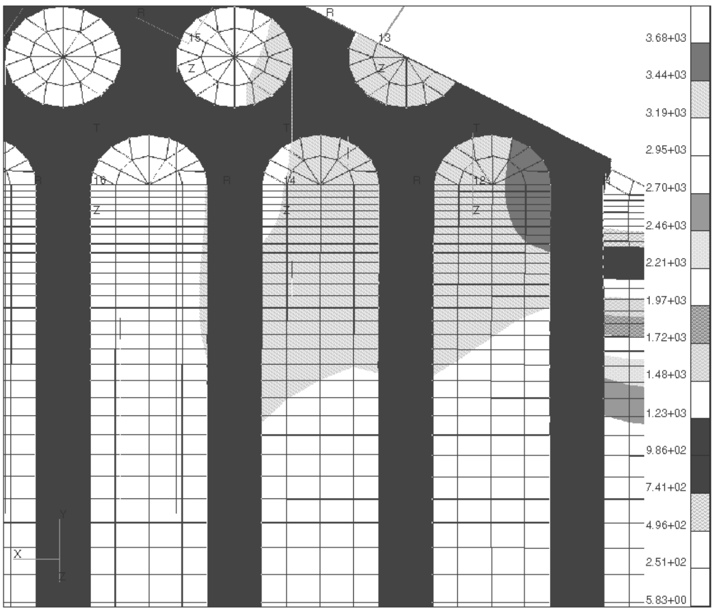

(c)

Fig. 2.3. (**a**) Optical image of Ti/SiC composite microstructure, (**b**) wedge section of model hexagonal distribution of fiber composite with boundary conditions for finite element analysis, and (**c**) a 30° wedge of finite element model showing the axial stress distribution in the fibers and matrix around a central broken fiber (reprinted with permission from [38])

Modeling of loading transfer through a fiber/matrix interface is a key step to properly simulate the stress distributions in the fibers. The interfaces can be classified into weak and strong bond interfaces according to interfacial bonding strength. If the fiber/matrix interface is strong, no interfacial debonding occurs. Modeling of such an interface is simple. Since there is no sliding between the fiber and matrix, the matrix and fiber elements are compatible and shear the same nodes at the interface in the finite element model. However, if the interfacial bonding is weak, the interface will debond, leading to sliding during loading. In this case, contact elements can be used to simulate stress transfer across the fiber/matrix interface. If the residual thermal stresses (axial tension in the matrix, axial compression in the fibers, and radial compression σ_r at the interface) are high, the fiber/matrix bond strength is usually assumed to be zero for simplification. Interfacial stress transfer is then realized by Coulomb friction at the interface so that the friction shear stress τ along the interface in the slip zone is simply $\tau = -\mu\sigma_r$, where μ is the coefficient of friction.

The introduction of a fiber break in the central fiber at the midplane of the model induces significant changes in the local stresses around the break (e.g., Fig. 2.3c). The stress distribution around a broken fiber is very complex. Multiscale modeling progresses by assuming that all of these details are not relevant to the desired macroscopic behavior. For the propagation of damage among fibers, the tensile stresses in the unbroken fibers drive the growth of preexisting flaws in those fibers if the tensile stress is large enough. It is assumed that it is sufficient to consider the average tensile stress through the cross-section of any fiber, rather than maintain the full spatial variation. While it is certainly true that any particular fiber can have a flaw that experiences a stress higher or lower than the average [20, 33], the influence of such an effect has not been considered. Condensing the detailed information from studies such as that shown in Fig. 2.3c, consider the stress in the broken fiber and the stresses in the surrounding fibers. The stress in the broken fiber is zero at the break point and recovers along the broken fiber, as shown in Fig. 2.4a. Shear deformation along the interface, by either shear yielding of a well-bonded plastically deforming matrix or frictional sliding along a debonded interface, leads to a nearly linear recovery of axial stress in the fiber. Figure 2.4b shows the average axial stress concentration factor (SCF = actual stress normalized by far-field applied fiber stress) in the plane of the fiber break on the successive sets of neighbors around the broken fiber. The stresses in the neighboring fibers are increased to compensate for the loss of load-carrying capacity in the broken fiber, with the SCF decreasing with increasing distance from

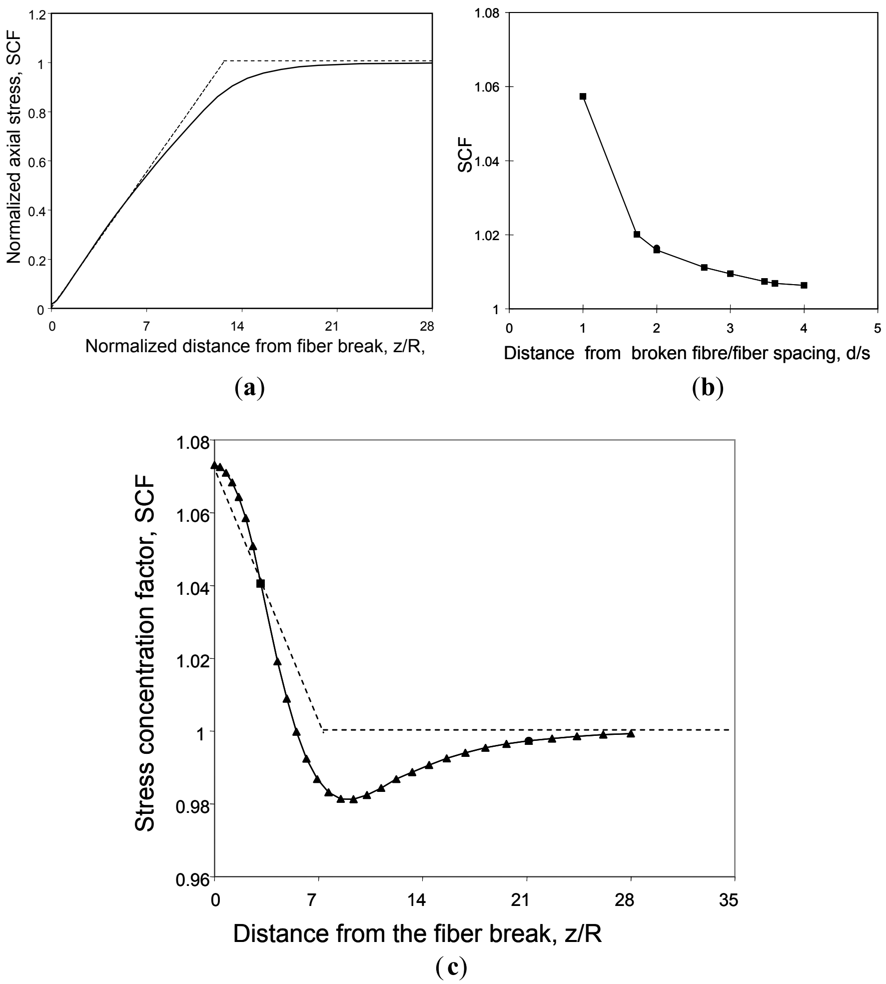

Fig. 2.4. (**a**) Axial stress distribution on the central broken fiber along the fiber direction z/R (R = fiber radius), normalized by the far-field fiber stress, (**b**) axial stress concentration factor (*SCF*) on the fibers as a function of the distance away from the broken fiber, normalized by fiber spacing s, and (**c**) average axial stress concentrations on the near-neighbor fibers along the fiber direction z. *Dashed lines* in (**a**) and (**c**) show the approximated stress concentrations using a constant interfacial shear stress τ model that is employed in one of the larger-scale models (Green's function model)

the broken fiber. The average stress concentration on the near-neighbor fibers vs. the distance z away from the crack plane is shown in Fig. 2.4c. Near the plane of the break, the neighboring fiber stresses are larger than in the far-field. Within increasing distance z, the broken fiber recovers its load-carrying capacity and the SCFs of the surrounding fibers thus decrease over a similar length scale. The SCF on the neighboring fibers can actually fall below unity before recovering to unity at larger distances, which is due to bending that arises from the need to satisfy compatibility. The details, such as those shown in Fig. 2.4, depend on the input constitutive properties: the fiber elastic modulus, the matrix elastic modulus and plastic flow behavior, if any, and the interface constitutive model. However, the results are generically those shown in Fig. 2.4, and the SCFs and length scales of stress recovery are the information derived from the detailed micromechanical model that is passed to a larger-scale damage accumulation model.

2.2.3 Mesoscale Modeling of Fiber Damage Evolution

The finite element (FE) models provide the detailed stress state around a single broken fiber. Larger clusters of broken fibers can be investigated, but such a direct numerical approach is limited to symmetric clusters of breaks due to the symmetry of the unit cell. Decreasing the symmetry of the unit cell is possible but computationally difficult. Furthermore, to understand the size scaling of the composite strength and, thus, predict strengths of very large samples, requires hundreds of simulations of failure in composites having several hundred fibers. Here, two alternative approaches to obtaining reasonably accurate but computationally more feasible results: the 3D shear-lag and Green's function methods are discussed. The goal of these methods is to reliably calculate the stress states in any surviving fibers given an arbitrary spatial distribution of fiber breaks, while capturing the proper SCFs and length scales computed from the detailed finite element method (FEM) models.

Shear-lag method

The shear-lag model (SLM) for fiber SCFs has a long history, dating back to the work of Hedgepeth and Hedgepeth and Van Dyke [4, 14, 15, 30]. In this model, the fibers are treated as one-dimensional extensional elements of modulus E_f while the matrix is treated as a material with modulus G_m that transfers tensile loads among fibers via shear deformation only and carries no tensile loads. Here we discuss a 3D SLM developed by Okabe and Takeda [25] that incorporates interface sliding due to friction and/or

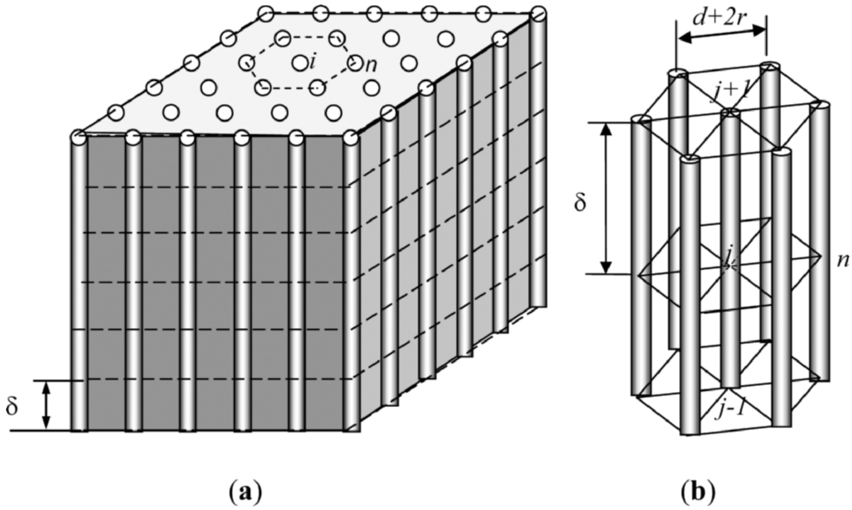

Fig. 2.5. (**a**) 3D model with 1D fibers and load transfer calculation in shear-lag and Green's function models and (**b**) the nodes around *i*th fiber

matrix yielding as well as evolving fiber damage in a single, compact framework. A schematic view of the composite with a hexagonal fiber array and relevant notation is shown in Fig. 2.5. The SLM assumes that the local matrix shear stress is governed by the smaller of (1) the elastic shear stress associated with the neighboring fiber displacements

$$\tau_{\mathrm{n}}(z) = G_{\mathrm{m}}[u_n(z) - u_i(z)]/d, \tag{2.1}$$

where u_n is the displacement of the nth near-neighboring fiber to fiber i (see Fig. 2.5) and d is the fiber spacing or (2) $|\tau_{\mathrm{n}}| = \tau_{\mathrm{y}}$, where τ_{y} is the yield strength for an elastic/perfectly plastic matrix or the debonded interfacial shear stress for a sliding interface. Within this framework, force equilibrium on the ith fiber in a hexagonal array with an elastic/plastic matrix is, when discretized by a uniform mesh size $\Delta z = \delta$, given by

$$\begin{aligned} &3AE_{\mathrm{f}}\left[\frac{a_{i,j}(u_i(z_{j+1}) - u_i(z_j)) - a_{i,j-1}(u_i(z_j) - u_i(z_{j-1}))}{(2 + a_{i,j} + a_{i,j-1})\delta^2}\right] \\ &\quad + h\sum_{n=1}^{6}\left[\frac{G_{\mathrm{m}}}{d}(u_n(z_j) - u_i(z_j))b_n + \tau_{\mathrm{y}}(1 - b_n)\right] = 0, \end{aligned} \tag{2.2}$$

where $u_i(z_j)$ is the displacement of the jth node of the ith fiber located at longitudinal position z_j, with $h = \pi r/3$ and $A = \pi r^2$. In (2.2), $a_{i,j}$ are damage parameters: $a_{i,j-1} = 0$ if the element of fiber i between z_{j-1} and z_j is broken, and $a_{i,j-1} = 1$ if unbroken; similarly, $a_{i,j} = 0$ if the element between z_j and z_{j+1} is broken, and $a_{i,j} = 1$ if unbroken. The b_n ($n = 1$–6) in (2.2) are yield indicator parameters, with $b_n = 1$ if $|\tau_n|$ is less than τ_y and $b_n = 0$ otherwise. Periodic boundary conditions are used on the lateral edges of the composite, so that all fibers have six neighbors. The boundary conditions for uniaxial loading are zero displacement at $z = 0$, $u_i(0) = 0$, and a constant applied displacement U at $z = L$, $u_i(L) = U$. The stresses in the unbroken fiber elements follow from Hooke's law as:

$$\sigma_i(z_j) = E_f[u_i(z_j) - u_i(z_{j-1})]/\delta. \tag{2.3}$$

The SLM predicts the stress concentration and recovery around an arbitrary collection of broken fibers, but the assumptions in the model are not always appropriate. Comparison of the SLM predictions against full finite element modeling for the exact same problem shows that the standard SLM can accurately predict the stress recovery length along a broken fiber for a wide range of fiber/matrix stiffness ratios [37]. However, the SCFs are only accurate for systems with a high fiber/matrix stiffness ratio and high fiber volume fraction; practically, this corresponds to polymer matrix composites with high fiber fraction. For other material systems, in particular metal matrix composites, factors such as the neglect of shear across the finite fiber dimensions in the SLM, the matrix load-carrying capability, and/or the loading history, makes the SLM less accurate for the stress transfer [37]. The stress transfer is more diffuse in the SLM than in the full FEM studies, making the SLM less conservative in predictions of local damage evolution. Thus, care must be taken in using the SLM to model composite deformation and failure, although applications to polymer composites with stiff fibers and high fiber volume fractions should be accurate and realistic.

Green's function model

The Green's functional model (GFM) [36] uses the in-plane SCFs around a single fiber break as obtained from any detailed numerical model as a Green's function, makes a simple approximation for the SCFs along the length of the unbroken fibers, and then computes the 3D damage evolution due to multiple, interacting fiber breaks.

Specifically, the data for in-plane SCFs, as shown in Fig. 2.4b, define a Green's function G_{ij} for stress transfer from broken fiber j to surrounding fiber i. The stress distribution around a broken fiber is then modeled by the simple constant τ SLM. In other words, for fiber m broken at position z_m^{b}, the stress along the broken fiber is approximated as

$$\sigma_m^{\mathrm{b}}(z) = 2\tau\left|z - z_m^{\mathrm{b}}\right|/r, \quad \sigma_m^{\mathrm{b}}(z) \le \sigma_m(z) \tag{2.4}$$

as shown in Fig. 2.4a, where $\sigma_m(z)$ is the axial stress in the fiber existing before the break, so that (2.4) is operative only within the slip length around the fiber break. The stress lost by the broken fiber at position z,

$$p_m(z) = \sigma_{app,m}(z_m^b) - 2\tau\left|z - z_m^b\right|/r \qquad p_m(z) \ge \sigma_m(z) \tag{2.5}$$

is transferred to the surrounding fibers using the Green's function computed in the plane of the break. With these two features, the total stress $\sigma_i(z)$ on unbroken fiber i in plane z due to broken fibers $\{m\}$ is approximated as

$$\sigma_i(z) = \sigma_{\mathrm{app},i}(z) + [G_{ik}(1-G)_{kl}^{-1}G_{lm}]p_m(z), \tag{2.6}$$

where $\sigma_{\mathrm{app},i}(z)$ is the applied stress on fiber i at position z and there is an implied sum over the repeated indices k, l, m. Equations (2.4)–(2.6) predict that the stress transferred to surrounding fibers decreases linearly with distance from the fiber break until the slip region ends. This approximation is shown in Fig. 2.4c, from which it is evident that the model captures the basic features of the deformation but misses the subtle details associated with bending and compatibility that arise in the full FEM and also in the SLM. By construction, however, the GFM always satisfies equilibrium of the axial load, i.e., the sum of the forces over any cross-section of the fiber system is equal to the total force applied across the section. Equations (2.4)–(2.6) are solved at a discrete set of points z_j along each fiber and, thus, provide the analog of the stresses emerging from the solution of (2.1)–(2.3) in the SLM. Since the GFM takes the input directly from a more detailed calculation, it has a wider range of applicability than the SLM. However, for cases where the SLM is a good approximation, such as polymer matrix composites, the GFM contains some additional assumptions that could modify the predictions. A comparison of the GFM vs. the SLM, when the SCFs from the SLM are used as the input to the GFM, shows that the GFM predicts damage evolution and tensile strength in good agreement with the SLM for the systems considered [36], thus suggesting that the approximations made in the GFM model are reasonable.

2.2.4 Predictions of Tensile Strength in Small Samples

The ultimate tensile strength of the composite is determined by two contributions. The first contribution is the fiber bundle strength σ_f^*, which is determined via simulation of the evolution of fiber damage and stress transfer from broken to unbroken fibers using the shear-lag or Green's function method in a stochastic simulation model to be described below. The second contribution is the load-carrying capacity of the matrix. Since the fiber damage that drives ultimate failure is fairly localized in space, in both the longitudinal and transverse directions, most of the matrix is deforming as if in an undamaged composite. Thus, to a very good approximation, the average stress carried by the matrix is the axial stress in an undamaged composite at a stress equal to the composite strength. The ultimate strength can thus be expressed as

$$\sigma_{\mathrm{uts}} = V_f \sigma_f^* + (1 - V_f)\sigma_m(\sigma_{\mathrm{uts}}), \tag{2.7}$$

where σ_m is the axial matrix stress and is a function of the applied stress. The main goal is to compute the fiber bundle strength σ_f^*.

For any fixed state of damage, i.e., spatial distribution of broken fibers, the SLM and the GFM compute the associated tensile stresses in all fibers in the system. Damage evolution then occurs by further failure of fibers due to the increasing stress concentrations. The progressive fiber damage occurs because the fibers have a statistical distribution of flaws within them, leading to a corresponding statistical distribution of strength on any set of fiber elements. Modeling of the damage evolution thus requires the appropriate fiber strength distribution as input. The cumulative probability of fiber failure $P_f(\sigma, L)$ in a gauge length L at stress σ is usually modeled as a Weibull distribution that accounts for the flaw-sensitive, weak-link nature of the brittle fiber failure. In a two-parameter Weibull model, $P_f(\sigma, L)$ is given by

$$P_f(\sigma, L) = 1 - \exp\left[-\frac{L}{L_0}\left(\frac{\sigma}{\sigma_0}\right)^m\right], \tag{2.8}$$

where σ_0 is a characteristic fiber strength for fibers of length L_0 and m is the Weibull modulus describing the statistical spread in strengths. For most commercial fibers, the fiber strength properties are well characterized by the two-parameter Weibull strength model. The Weibull parameters σ_0 and m are usually obtained from experiments in which a large number of fibers of length L_0 are tested in tension prior to incorporation into the composite.

However, composite processing can damage the fibers, modifying the in situ strength distribution compared to the initial ex situ distribution. To address this problem, fibers can sometimes be extracted from as-processed composites and then tested to obtain the appropriate strength parameters [11]. Another approach is to examine the fracture mirrors on fibers protruding from the fracture surface of a tested composite, from which the fiber strength statistics can be derived [7]. In any case, simulations of composite tensile strength require accurate knowledge of the in situ fiber strength distribution.

Within the constant τ shear model for interface sliding, an analytic model that ignores local stress concentrations, the so-called *Global Load Sharing model*, permits for the identification of a characteristic stress that embodies most of the major dependencies of composite behavior on fiber and interfacial characteristics [6, 7]. This characteristic stress σ_c is the characteristic fiber strength at a characteristic length δ_c, $P_f(\sigma_c, \delta_c) = 0.632$, and these interrelated quantities are given by [6]

$$\sigma_c = \left(\frac{\sigma_0^m \tau L_0}{r} \right)^{1/(m+1)}, \quad \delta_c = \frac{r\sigma_c}{\tau}. \tag{2.9}$$

In a simulation model, it is often convenient to normalize all lengths by δ_c and stresses by σ_c, using an appropriate value of τ to define the length δ_c. Even if τ is approximate, (2.9) condenses some of the major physical dependencies of the composite failure into two key parameters.

With the above preliminaries, the computation of the fiber bundle strength σ_f^* is straightforward. The simulation algorithm proceeds as illustrated in Fig. 2.6. A simulation model contains a computationally tractable number of fibers (typically ~1,000) each of length $L \geq 2\delta_c$. Each fiber is discretized into a series of small elements of length $\bar{\delta} \ll \delta_c$, as illustrated in Fig. 2.5. Each fiber element is then assigned a tensile strength at random from the Weibull distribution, i.e., a random number R in the interval [0, 1] is selected; and the strength of the element is assigned to be $\sigma_c (\delta_c / \bar{\delta})^{1/m} (-\ln(1-R))^{1/m}$. An initial tensile load is applied to the fiber bundle, and fiber breaks are introduced into those fiber elements for which the applied stress exceeds the assigned element strength. After these fibers break, the stress redistribution is calculated with the shear-lag or Green's function model. Under the redistributed stress, some fiber elements may then exceed their assigned strengths and are broken; and the stress redistribution is computed again. This fiber break and stress redistribution

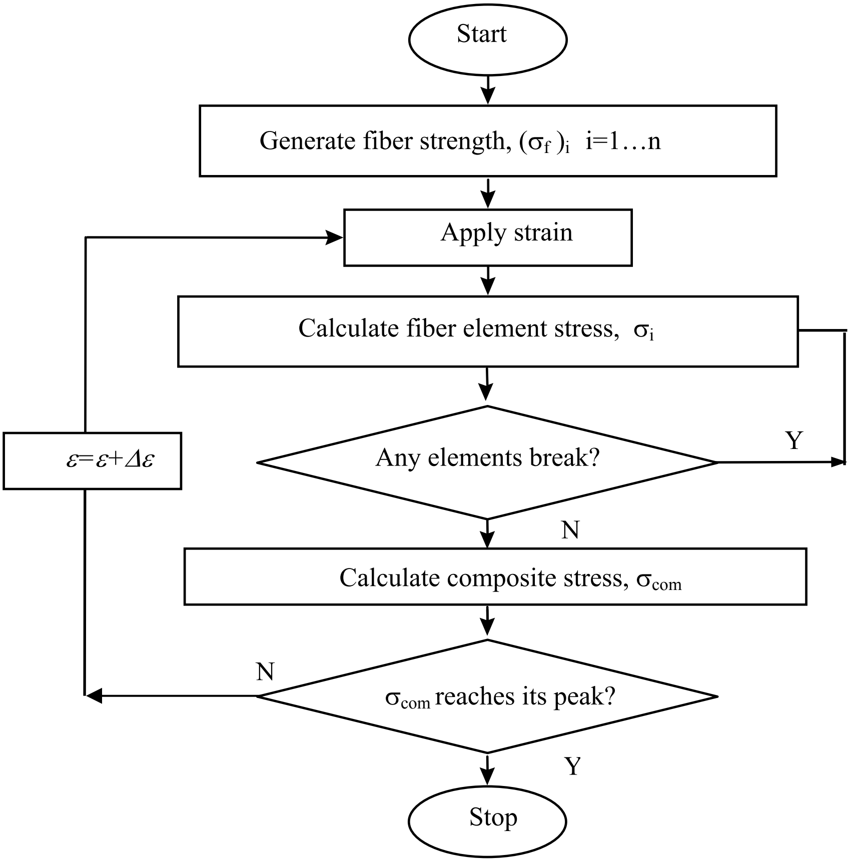

Fig. 2.6. Flow chart of simulation procedure for fiber damage evolution in fiber composites

process is repeated until no further fiber breaks are found; the damaged composite is then in a stable equilibrium state. The applied displacement or load is then increased by a small increment, and the above process is repeated. In the SLM, which is typically displacement controlled, the tensile strength is identified as the maximum stress. In the GFM, which is load controlled, the system undergoes catastrophic failure (all fibers break in some narrow range of the sample cross-section) at the tensile strength.

Figure 2.7 shows an example of the simulated stress–strain curve for an Al_2O_3/Al composite. The fiber damage evolution in the ultimate failure plane is shown via examination of the fiber SCFs in Fig. 2.7 at two stages: just at failure and just beyond failure. In Fig. 2.7, SCF values less than one indicate that the fiber is broken somewhere within a slip length of the failure plane and is carrying a reduced stress in the failure plane due to slip (2.4) while SCF values exceeding one indicate enhanced stresses on unbroken fibers in the plane of view. At low stress levels, isolated breaks occur at weak fiber elements throughout the material, and the stress concentrations are not sufficient to drive further failure. With increasing load, clusters of fiber breaks form due to both statistics and to enhanced local stresses. The stress concentrations around these clusters grow with the cluster size, driving further damage. When the load just reaches the tensile strength (Fig. 2.7a), a "critical" cluster of fiber breaks forms, consisting of a dispersed group of fiber breaks leading to local stress enhancements on the unbroken fibers in and around these breaks. With no further increase in applied load, fiber damage continues unabated spreading outward from the critical damage cluster. Figure 2.7b shows the damage configuration after some extent of unstable fiber damage. After some sporadic growth, the damage cluster becomes roughly penny shaped with very high-stress concentrations on its perimeter that drives the continued growth, similar to crack growth in a monolithic material.

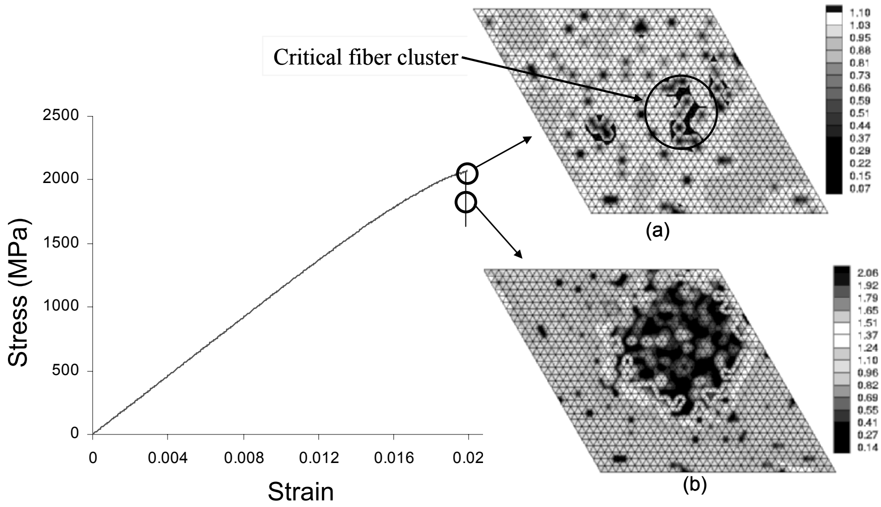

Fig. 2.7. Predicted stress–strain curve for an alumina fiber/aluminum composite with a matrix yield strength of 100 MPa, with schematics of fiber damage and stress concentrations in the plane of final fracture: (**a**) just at the failure strength, where a critical damage cluster can be identified and (**b**) after some unstable damage propagation at the failure strength, where the damage has formed a near penny shape crack. Each node corresponds to a single fiber (reprinted with permission from [35])

If either the fiber Weibull modulus or SCF is low, the composite can fail in a mode different from that described above. Figure 2.8a,b shows the failure process for an Al matrix composite with a lower matrix yield stress (σ_y = 50 MPa). In this case, the SCFs for individual breaks are lower leading to damage that is more uniformly distributed in the cross-section, as compared to Fig. 2.7a, such that a critical cluster cannot be identified in Fig. 2.8a. Even after unstable damage propagation (Fig. 2.8b), the damage still spreads quite uniformly through the cross-section. Thus, the SCF determined at the microscale by interface and matrix deformation plays a key role in determining the evolution of the damage, the formation of a critical damage cluster, the mode of damage, and, ultimately, the statistics and size scaling of the tensile strength.

The composite failure strength has a statistical distribution. By performing many simulations, with each simulation giving a different strength due to the different random fiber strengths and evolution of the damage clusters, the distribution can be determined numerically. The strength distribution depends mainly on the fiber Weibull modulus *m* and the SCFs. High *m* and/or high SCFs result in more localized damage (Fig. 2.7) and broader distributions while low Weibull modulus and/or low SCFs lead to more dispersed damage, as show in Fig. 2.8, and narrower distributions of strength. Thus, the strength is a combination of the spread in fiber strengths (*m*) and the SCFs [35]. The size scaling of the composite strength for material systems discussed below depends on the combination of fiber Weibull modulus and SCF.

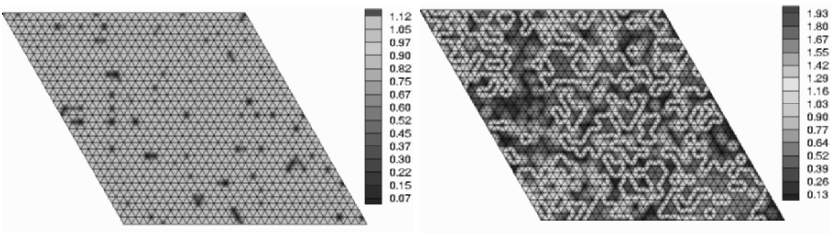

(**a**) (**b**)

Fig. 2.8. Fiber damage and stress concentrations in the plane of final fracture in alumina fiber/aluminum composites. Each node point corresponds to a single fiber. (**a**) For σ_y = 50 MPa, just at the failure strength, where there is no clear localization of damage and (**b**) after some unstable damage propagation at the failure strength, with the damage still distributed across the entire sample cross-section (reprinted with permission from [35])

2.2.5 Size-Scaling Model at Large Scale

The composite tensile strength decreases with increasing sample size. This is due to the underlying dependence of the fiber strengths on length. However, since a number of fibers must fail locally in the composite to create a critical cluster capable of driving macroscopic failure, the statistical distribution of composite strengths at fixed size is much narrower than that of the single fiber. Similarly, the size scaling of the characteristic composite tensile strength is much weaker than that for the individual fibers [13]. Size scaling is an important issue because it bridges the scales between numerical simulation sizes and test specimen and/or component sizes. Size scaling is also intimately linked with reliability, i.e., the probability distribution of failure at any fixed size.

Since the composite strength is controlled by a weak-link failure, i.e., failure is driven by the formation of a localized cluster of damage somewhere in the material and much smaller than the sample size for large samples (see Fig. 2.7), information on the cumulative probability distribution of the fiber bundle strength at a fixed size $P_{n_\mathrm{s}}(\sigma)$ can be used to obtain the characteristic $\tilde{\sigma}$ vs. the size as follows. First, the "size" involves the number of fibers n_f in the cross-section and the length of the sample L. Failure occurs within a longitudinal section length of $\sim\delta_\mathrm{c}$, and so the sample length L can be viewed as consisting of a set of $L/(0.4\delta_\mathrm{c})$ independent "bundles," where the factor of 0.4 has been derived from detailed statistical analysis of simulations and analytic estimates [26]. The size of the composite is then $n = n_\mathrm{f} L/(0.4\delta_\mathrm{c})$. Now, the characteristic strength $\tilde{\sigma}$ at any size n satisfies $P_n(\tilde{\sigma}) = 1 - \mathrm{e}^{-1}$. Furthermore, weak-link scaling dictates that the probability distributions for samples of sizes n and n' are related via

$$P_n(\sigma) = 1 - \left(1 - P_{n'}(\sigma)\right)^{n/n'} . \tag{2.10}$$

Using the simulation data $P_{n_\mathrm{s}}(\sigma)$ at size $n' = n_\mathrm{s}$ on the right-hand side of (2.10) and setting the left-hand size equal to $1 - \mathrm{e}^{-1}$, we find that the size n having characteristic fiber bundle strength $\tilde{\sigma}$ must satisfy

$$n = -n_\mathrm{s} / \ln\left(1 - P_{n_\mathrm{s}}(\tilde{\sigma})\right), \tag{2.11}$$

which then implicitly generates the strength vs. size, $\tilde{\sigma}(n)$.

To investigate the size scaling of composite strength numerically within the present model, we need to perform a large number of simulations on composites containing n_s fibers using the model described in Sect. 2.1. From these simulations, we directly obtain the cumulative probability distribution $P_{n_s}(\sigma)$ for failure of the fiber bundle at the simulated size n_s. The composite strength then follows directly from (2.11).

2.3 Case Studies: Prediction of Strength by the Multiscale Coupling Approach

An approach to the hierarchical modeling of composite tensile failure has been presented. The proposed multiscale modeling involves the passing of key information from smaller to larger scales. In this section, the general multiscale modeling approach will be implemented to predict the properties and performance of several different composite systems under tensile loadings. Although the microstructures in fiber-reinforced composites are similar, the fiber/matrix interfaces are quite different, and load transfer strongly depends on the interfacial bonding strength. In the case of a weak interface, debonding will occur when the fiber breaks with the subsequent deformation controlled by a frictional interfacial shear stress. Matrix yielding also plays an important role in the failure of the composites. High yielding matrices may bear significant loading, for instance, in metal matrix composites. In the absence of debonding, the matrix shear yield stress can determine the "sliding" behavior after a fiber breaks. Here, metal and polymer matrix composites will be used as examples to demonstrate how to predict the tensile strength of macroscopic composite samples from the detailed micromechanics.

2.3.1 Polymer Matrix Composites (PMCs)

Polymer composites reinforced by carbon or glass fibers have high strength and are widely used as high-performance materials in aerospace, electronics, and infrastructures. Here the multiscale modeling approach is used to predict the strength of fiber-reinforced polymer composites by linking composite microstructure and mesoscale fiber damage evolution to the mechanical properties at very large scale.

The stress concentration predicted by the shear-lag model and finite element model has been compared. The results show, for both the elastic and elastic–plastic cases, that the SLM agrees with the finite element predictions very well except for a region very near the fiber break, nearly independently of the fiber break load for polymer matrix composites with high fiber volume fraction [37]. In this case, the SLM is reliable for predicting the stress concentration in the fibers. Hence, the SLM is used with the mesoscale Monte Carlo damage evolution model following the standard procedure described in Sect. 2.2.

The composite material studied here is a plastic matrix reinforced by carbon fibers. The thermomechanical properties of the carbon fibers and polymer matrix are presented in Table 2.1. The fiber strength is described using a modified two-parameter Weibull model: $P_{\mathrm{f}}(\sigma, L) = 1 - \exp[(L/L_0)^{\alpha}(\sigma/\sigma_0)^{m}]$, where $\alpha = 0.7$ is the fitting parameter from the experimental results for the carbon fiber [24]. The simulated composite is composed of 1,024 fibers of length $4\delta_{\mathrm{c}}$in a hexagonal array with periodic boundary conditions. Each fiber is divided into 100 longitudinal elements to minimize discretization errors.In the absence of fiber damage, uniaxial loading determines the overall stress–strain response of the undamaged composite. Due to the very low matrix yield stress and high fiber strength and stiffness, the stress–strain behavior is nearly linear over the entire range of loading. If a fiber breaks during loading, the shear stress in the matrix near the fiber break may exceed the shear yield strength, leading to matrix yielding. The possibility of interface debonding, which can follow after matrix yielding, is neglected; debonding can be included and is neglected only for simplicity.

Table 2.1. Thermoelastic parameters of fiber and matrix [24]

Property	Fiber	Matrix
Fiber radius, r (μm)	2.5	–
Elastic modulus, E (GPa)	294	3.4
Fiber volume fraction, V_{f}	0.6	
Poisson's ratio, ν	0.22	0.345
Weibull modulus, m	3.8	–
Weibull strength, σ_0 (MPa) at L_0 = 50 mm	3,570	–
Yield shear strength, σ_{y} (MPa)	–	52.4

With the model and parameters noted above, 1,000 simulation studies of composite failure have been performed. From these simulations, the probability distribution $P_{n_{\mathrm{s}}}(\sigma)$ for failure of the fiber bundle at the simulated size n_{s} is directly obtained, as shown in Fig. 2.9. Applying the size-scaling theory (2.11), the strength of large composites comparable to the sizes tested experimentally, which contain 10^4–10^6 fibers with a gauge length of 10 mm is obtained. Figure 2.10 shows the experimental and predicted fiber

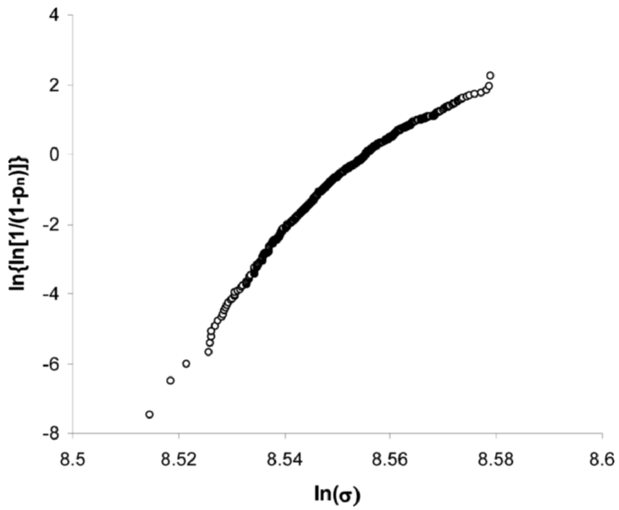

Fig. 2.9. Distribution of fiber bundle strengths (MPa) in a unidirectional CFRP composite containing 1,024 fibers of length $4\delta_c$, plotted in Weibull form

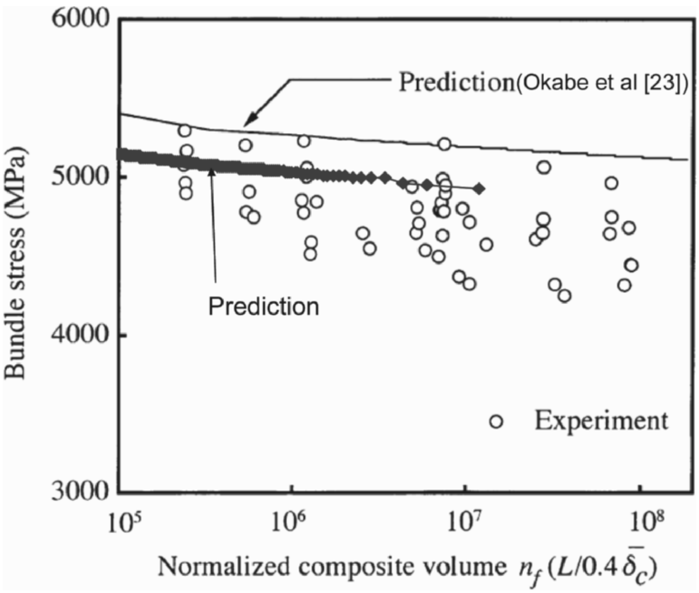

Fig. 2.10. Fiber bundle strength $\sigma_f^* = (\sigma_{uts} - \sigma_m)/V_f$ vs. linear composite size (number of fibers n_f times fiber length L), as predicted by simulations and as obtained experimentally (reprinted with permission from [24])

bundle strength vs. composite volume (n). The predicted strengths fit the experiments very well. Okabe et al. also predicted the strength using a similar method but with a modified Weibull distribution model (Weibull of Weibull (WOW) statistics) for fiber strength [24] and obtained strengths very close to those predicted.

2.3.2 Metal Matrix Composites (MMCs)

Al_2O_3/Al composite

We first consider an aluminum alloy reinforced by Al_2O_3 fibers. The thermomechanical properties of the fibers and aluminum alloy are presented in Table 2.2. Due to chemical bonding, the Al/Al_2O_3 interface is strong and debonding does not occur before matrix yielding. Unlike polymer matrix composites, however, the Al matrix has a much larger elastic modulus and, hence, can exhibit wide-spread yielding. The matrix can also carry significant loads around a broken fiber. Because of low fiber/matrix stiffness ratio, the discrepancy between the shear-lag model and the finite element model stress concentrations in the Al_2O_3/Al composite is significant [37]. Therefore, the Green's function method is used to accurately represent the stress concentrations derived from direct, small-scale finite element analyses results.

A range of yield strengths for the Al alloy (50, 100, and 200 MPa) is considered to examine possible effects of alloying, in situ aging, etc. that may prevail in the as-processed composite. Similar to the polymer matrix composites, uniaxial loading determines the overall stress–strain response of the undamaged composite in the absence of fiber damage. Above an applied composite stress of 500 MPa, the matrix is fully plastic.

Table 2.2. Thermoelastic parameters of fiber and matrix for Al MMC [35]

Property	Fiber	Matrix
Fiber radius, r (μm)	6	–
Elastic modulus, E (GPa)	390	70
Poisson's ratio, ν	0.22	0.345
Fiber volume fraction, V_f	0.65	
Thermal expansion coefficient, α (10^{-6} per °C)	6.5	24
Weibull modulus, m	9	–
Weibull strength, σ_0 (MPa) at L_0 = 1 m	2,060	–
Yield strength, σ_y (MPa)	–	50, 100, 200

The 3D FEM to obtain information on deformation around fiber breaks. Introducing a fiber break into the central fiber at the midplane of the FEM model induces significant changes in the local stresses. Figure 2.11a shows the shear stress distribution along the broken fiber for different matrix yield strengths at a load of 1,000 MPa. At a low yield strength (σ_y = 50 MPa), the shear stress in the plastic zone is essentially $\sigma_y / \sqrt{3}$. For higher σ_y, the shear stress shows more spatial variation but is still about $\sigma_y / \sqrt{3}$ on average. Figure 2.11b shows the average axial stress within the broken fiber along the fiber length at an applied stress of 2,000 MPa. As expected by equilibrium requirements, the stress recovers nearly linearly when the shear stress is nearly constant and then increases more slowly as the shear stress decreases to zero. The "slip" or "stress recovery" length around the broken fiber can be estimated using the simple shear-lag model and a constant interfacial shear stress τ, as indicated in Fig. 2.11b; the corresponding τ values are shown in Table 2.3. To capture the major effects of the in-plane stress redistribution, the average SCF (averaged over the fiber cross-section) is considered, as shown in Fig. 2.11c. The spatial extent of load redistribution varies with yield strength: the SCF of the near-neighbor fibers increases with increasing σ_y and the spatial range decreases. Since the matrix carries load, the SCFs are smaller than those in carbon fiber-reinforced polymers. Simulations are performed for a composite with 1,024 fibers of length L = 10 mm to obtain a statistical distribution of tensile strengths. The tensile strength of small size samples can be predicted directly via (2.7) using the mean strength obtained from many simulations of the fiber bundle strength. Such strengths, for the different matrix yield strengths, are shown in Table 2.3. The predictions are relatively insensitive to the value of the yield strengths due to a combination of factors although the mode of failure is quite different, as shown in Figs. 2.7 and 2.8. An increased σ_y, and hence increased τ, increases the characteristic strength and the fiber bundle strength as $\tau^{1/(m+1)}$, and increases the matrix contribution to the strength. However, increased τ also leads to increasing SCFs that are more localized on the nearest fibers, which drives the formation of larger damage clusters at lower loads and decreases the composite strength. In the present case, these competing factors cancel one another to a large degree, leading to a slow increase in composite strength with increasing τ. Since the SCF depends on other constitutive properties and the fiber damage evolution depends on the strength distribution, the cancellation is also a function of features such as the fiber/matrix elastic mismatch, the fiber diameter, and fiber Weibull modulus.

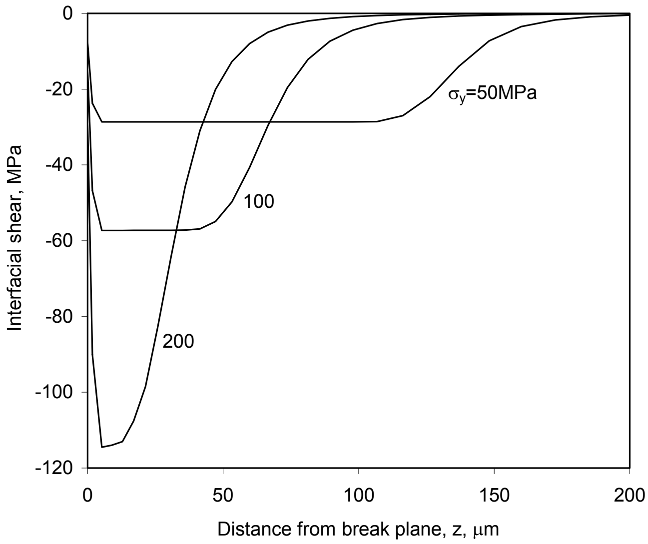

(a)

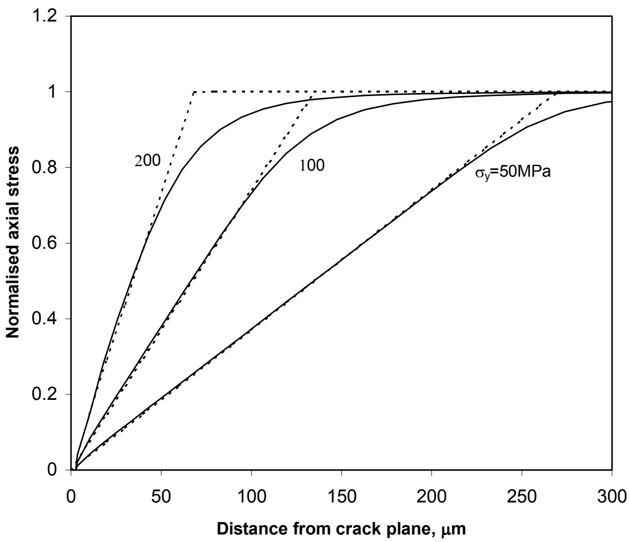

(b)

Fig. 2.11 (continue)

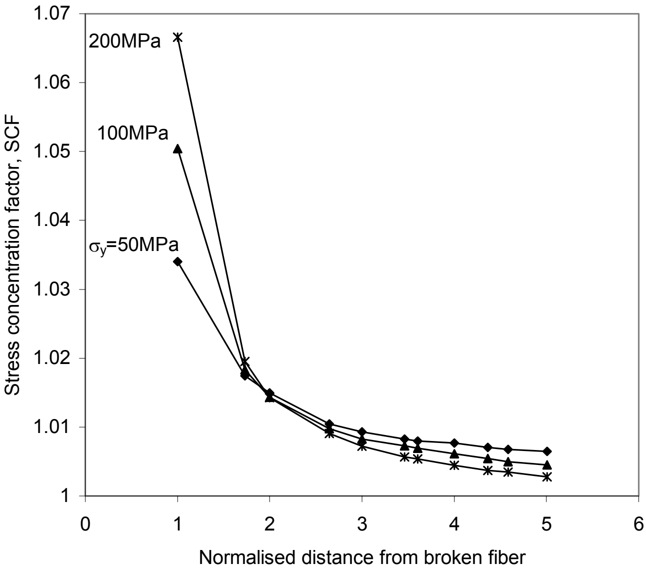

(c)

Fig. 2.11. (**a**) Interfacial shear stress along a broken fiber at an applied stress of 1,000 MPa for different matrix yield strengths, (**b**) axial stress distribution on a broken fiber along the fiber direction *z*, normalized by the far-field fiber stress, at an applied stress of 2,000 MPa for different matrix yield strengths, and (**c**) axial stress concentration factor (*SCF*) on nearby fibers vs. distance from the broken fiber, normalized by the fiber spacing *s*, at an applied stress of 2,000 MPa for different matrix yield strengths. *Dotted lines* show constant τ "shear-lag" fit to the data (reprinted with permission from [35])

Table 2.3. Parameters and tensile strength, as measured and as predicted [35]

Parameters	Prediction[a]			Experiment
Matrix yield strength, σ_y	50	100	200	100
Interfacial shear stress, τ (MPa)	32.5	65	125	–
Typical maximum stress, σ_c (MPa)	4,527	4,852	5,200	–
Average fragment length, δ_c (μm)	824	447	248.6	–
Tensile strength, σ_{uts} (MPa)	2,178	2,347	2,496	2,051 ± 141

[a]Average value of 20 results on 1,024 fibers of gauge length $L = 10$ mm.

Experiments on the current material system have been performed by Ramamurty et al. [28] using three-point, four-point, and tension loadings. Only the size of the tension test can be determined directly; the effective volumes tested in bending depend on the Weibull modulus of the composite strength distribution, which is not known a priori. Ramamurty et al. considered the measured scaling of the mean strengths to derive a composite Weibull modulus of about 55, which was then used to assign effective composite volumes to the three- and four-point bend test strengths. The four-point tests were deduced to have an effective size of about 12,000 mm of total fiber length (number of fibers times length of fibers). This matches the volume of 10,240 mm (1,024 fibers of length 10 mm) in the simulations performed rather closely. Hence, the quoted experimental strength in Table 2.3 is that for the four-point bend test. The agreement is quite reasonable, with a difference of ~10% for the yield stress of 100 MPa, which is close to that pertaining to the experiments. Some of the difference could be due to processing-induced fiber damage, such that the ex situ values are not directly applicable to the in situ fibers. Some of the difference may also be due to the influence of bending strain gradients, which is neglected in assuming that failure is driven by locally uniform tensile loading.

To investigate the size scaling of composite strength numerically, extensive simulation studies were performed on larger composite sizes. Specifically, 1,000 simulations were performed on composites containing 1,024 fibers of length 5 mm. From these simulations and (2.7), we directly obtain the probability distribution $P_{n_s}(\sigma)$ for failure of the composite at the simulated size n_s. Figure 2.12 shows the composite strength σ_{uts} vs. composite size $n_f L$ (n_f fibers each of length L), as obtained from the simulation data and (2.11), demonstrating the decreasing strength with increasing composite size. Also shown in Fig. 2.12 are the results of Ramamurty et al. at the estimated test sizes. The predicted strength decreases but more slowly than found experimentally, leading to a difference of ~27% at the largest size.

There are several possible reasons for this discrepancy, all of which lie at the micromechanical fiber/matrix/interface scale. First, the matrix deformation around the fibers is very large. Thus, the details of matrix hardening may be important in determining the stress redistribution. Moderate strain hardening typical of many Al alloys leads to an increase in the local SCF, which drives more localized damage, smaller critical clusters at failure, lower strengths, and an increasing size-scaling effect. This points to the necessity of understanding the matrix constitutive behavior in even more detail than done here to properly capture the SCFs. Okabe et al. recently used the spring element model (a microscale model similar to SLM) coupled with the size-scaling model to predict the composite strength. In their calculation, they used an elastic–plastic hardening matrix

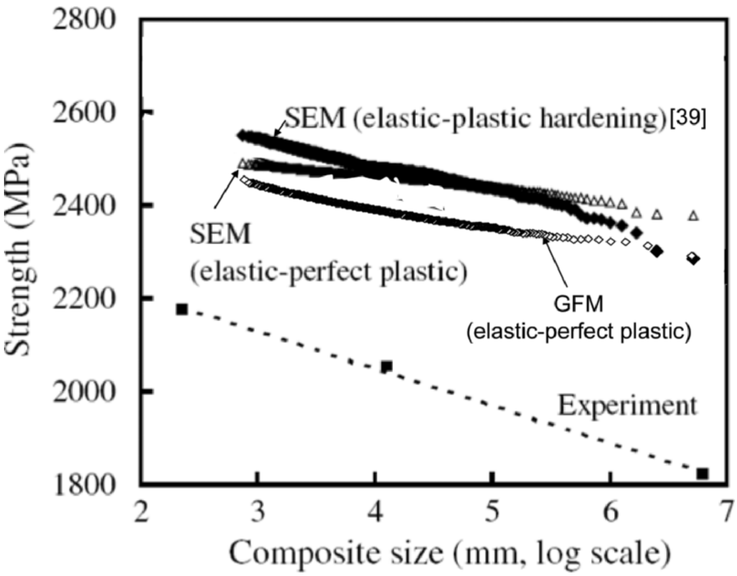

Fig. 2.12. Composite strength vs. linear composite size (number of fibers n_f times fiber length L) for an Al/Al_2O_3 metal matrix composite, as predicted by simulations (GFM and SEM (Spring element model) from [25]) and as obtained experimentally [28]

instead of a perfect plastic matrix [23]. The results in Fig. 2.12 show that, compared with the perfect plastic case, the strength with a strain-hardening matrix decreases quickly with size and is consistent with the experimental trend. Second, the Al matrix may undergo ductile failure locally, which would significantly affect the load transfer. In particular, if matrix "cracks" extend up to the neighboring fibers, then there will be additional local stress concentrations on regions of the neighboring fibers. Similar stress concentrations for sliding interfaces have been calculated in other materials and the influence on enhanced local fiber failure has been assessed [33]. For high interfacial sliding or shear yield stresses and high fiber Weibull moduli, the local stress concentrations can lead to a weaker composite and a more planar fracture surface (typical of Al MMCs). Methods to account for this effect within the mesoscale simulations described here have been addressed in [38]. Third, for MMCs, it is possible that matrix fracture could occur once the damage cluster gets close to critical and this might then trigger fracture. As a result, the strength would be different than predicted here. Such matrix fracture effects can be included in the Green's function model, as will be discussed in Chap. 4.

SiC/titanium composite

The SiC/Ti composites considered here were fabricated via magnetron sputtering of the matrix onto the fibers followed by isostatic pressing of the matrix-coated fibers into a composite [18]. This technique yields a nearly ideal hexagonal fiber distribution (Fig. 2.3a). The fiber volume fraction is 0.4. The interface is weak and debonds readily upon fiber fracture, and the interfacial sliding resistance in the as-fabricated composite is 55–75 MPa, as measured by pushout testing. Other thermomechanical properties are shown in Table 2.4. The SCS-6 fiber is represented by a homogeneous anisotropic material with elastic constants. The homogeneous Young's modulus E_f of the fiber is determined by fitting the rule of mixtures to a full 2D model. The elastic properties of the matrix are also shown in Table 2.4. The stress–strain behavior of the IMI834 Ti alloy as determined experimentally is very accurately represented by a Ramberg–Osgood relationship of the form

$$\varepsilon_m = \sigma_m / E_m + (\sigma_m / B)^{1/b}, \tag{2.12}$$

with $b = 0.0384$ the hardening exponent, $B = 1{,}229$ MPa the hardening coefficient, and E_m the matrix elastic modulus. The yield strength of the alloy is 950 MPa.

The multiscale modeling of composite strength starts from a micron-scale finite element model. A 3D finite element representation of the composite was constructed using symmetry to calculate the stress distributions around broken fibers. The model consists of 13,922 elements, including 3,255 gap elements and 13,888 nodes. The fiber/matrix bond strength is assumed to be zero. Coulomb friction at the interface $\tau = -\mu\sigma_r$ is assumed. For the cooling range shown in Table 2.4, $\sigma_r = 208$ MPa, leading to interfacial shear stresses ranging from 52 to 187 MPa for the range $0.25 \le \mu \le 0.9$. The finite element results show that the load transfer in metal matrix is affected by the matrix. Similar to the polymer matrix composites, the near-neighbor fibers bear most of the load and bear an increasing portion of the load as the friction coefficient increases. However, the surviving fibers do not take on all of the loads from the broken fiber. The fibers carry only 83% of the load at low coefficient of friction ($\mu = 0.25$) and only 64% of the load at high coefficient of friction ($\mu = 0.9$). The matrix carries the remainder of the load. Finite element results show that there is a clear axial stress concentration in the matrix near the broken fiber, which increases with increasing friction coefficient. The increased axial matrix stress occurs due to both hardening and constraint effects that govern the yielding. Similar calculations for an elastic/perfectly plastic matrix (no hardening) show similar increases in axial matrix load attributable purely to constraint effects. For a high coefficient of friction, $\mu = 0.9$, the stress in the matrix near the fiber break exceeds the tensile strength of the matrix so that a fiber break may actually cause matrix fracture. Matrix fracture can then induce a different and much more dangerous mode of composite fracture in which fiber and matrix fracture progress unstably from around a single break, since the load carried by the cracked matrix will be transferred predominantly onto the nearby fibers. This failure mode is in contrast to the distributed damage and failure that occurs when the matrix does not fail. Most existing models for stress transfer neglect the stress carried by the matrix and the possibility of matrix fracture.

Table 2.4. Thermoelastic parameters of fiber, matrix, and composite [38]

Material	E_{zz} (GPa)	$E_{rr} = E_{\theta\theta}$ (GPa)	$G_{r\theta}$ (GPa)	$G_{\theta z} = G_{zr}$ (GPa)	$\nu_{r\theta}$	$\nu_{\theta z} = \nu_{zr}$	α_{zz} (10^{-6} per °C)	$\alpha_{rr} = \alpha_{\theta\theta}$ (10^{-6} per °C)	ΔT[a] (°C)
Fiber	400	240	70	118	0.15	0.25	6.48	6.48	750
Matrix[b]	120				0.3		11.24		750
Composite	232	155	64	91	0.186	0.296	8.05	9.4	750

[a]Temperature difference for cooling from processing.
[b]Isotropic material.

Table 2.5. Thermoelastic parameters of SiC (SCS-6) fiber

Fiber radius, r (μm)	71
Elastic modulus, E_{zz} (GPa)	400
Weibull modulus, m	17
Weibull strength, σ_0 (MPa) at $L_0 = 25$ mm	4,580

Neglecting the possibility of matrix failure, the damage evolution during loading is simulated using the Green's function model with the SCFs around a broken fiber for different coefficient of friction calculated using the finite element model. The fiber parameters are listed in Table 2.5. The simulation method requires an appropriate value of τ to define the length δ_c and characteristic strength σ_c. The characteristic stress σ_c and characteristic length δ_c for different coefficient of friction are listed in Table 2.6.

Table 2.6. Parameters and tensile strength, as measured and as predicted [38]

Parameters	Prediction[a]			Experiment
Coefficient of friction, μ	0.25	0.5	0.9	–
Interfacial shear stress, τ (MPa)	51.7	103.5	186.3	55–75
Characteristic stress, σ_c (MPa)	4,946.4	5,141.6	5,313.0	–
Average fragment length, δ_c (μm)	6,792.9	3,527.1	2,024.8	–
Tensile strength, σ_{uts} (MPa)	2,268.0	2,317.5	2,344.5	2,200–2,300

[a]Average value of 20 results (Gauge length L = 20 mm, the number of fibers = 210).

The tensile strengths were predicted using the mean of many simulations of the fiber bundle strength σ_f^* and are shown in Table 2.6 for several different friction coefficients. The predictions contain no adjustable parameters and are in excellent agreement with the experimental data for the range of friction parameters consistent with the experimentally measured interfacial shear sliding stress [18]. The relative insensitivity of the predictions to the value of the friction coefficient is due to the same combination of factors as discussed previously for the Al MMCs.

Similar to Al matrix composites, the size scaling of composite strength was investigated numerically within the present model. One thousand simulations were performed on composites containing 1,000 fibers of length $4\delta_c$ (size $n_s = 4{,}000\delta_c$). The probability distribution $P_{n_s}(\sigma)$ for failure of the fiber bundle at the simulated size was directly obtained from these simulations. The results show that the tensile strength at the sizes of typical Ti MMC components ($\approx 10^6$ mm^3) is reduced by about 100 MPa below the value obtained on the small laboratory test coupons ($\approx 10^2$ mm^3). Currently, no experimental data are available to test the accuracy of the predicted scaling of strength with composite size.

2.4 Extension to Low-Cycle Fatigue of Titanium Matrix Composite

In highly stressed rotating components where Ti MMCs might be employed, the transient loadings associated with start-up/shutdown and maneuvering give rise to a situation where low-cycle fatigue dominates. Studies of low-cycle fatigue behavior of unnotched specimens indicate that matrix cracks in TMCs initiate at the matrix/fiber interface, fiber breaks, and surface flaws of the specimens and grow perpendicular to the fibers. The range of fatigue crack growth can be divided into a short crack range, a steady-state range, and composite failure [1, 2]. After an initial growth in the short crack range, the crack growth rate reaches a constant value (steady-state regime) due to fiber bridging that substantially shields the crack tip from the applied stresses. However, the high stresses in the bridging fibers can cause them to fail and ultimately drive the composite to fail catastrophically [3, 32].

Here, we extend the multiscale coupling approach to predict the low-cycle fatigue of Ti/SiC composites. We combine detailed finite element models of the stress states in and around small matrix fatigue cracks with the Green's function model to capture the stochastic fiber damage under the calculated stress states. Figure 2.13 illustrates the multiscale modeling procedure for low-cycle fatigue life predictions. The micromechanical finite element model provides both the crack tip stress intensity (ΔK_{eff}) governing fatigue crack growth and the stress distributions on the fibers in and around the fatigue crack. The Green's function model evaluates the failure of the fibers under the given stress state, distributes the stress from broken

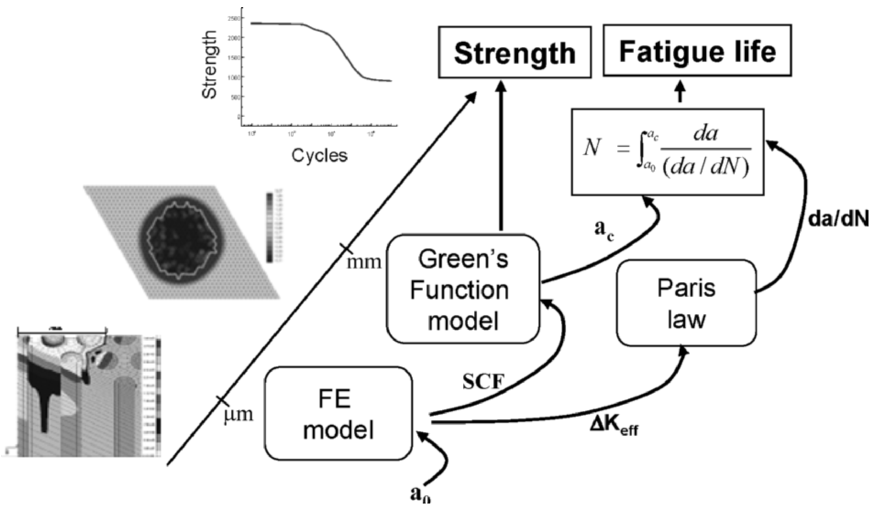

Fig. 2.13. Multiscale modeling of low-cycle fatigue of Ti/SiC composites

fibers onto the remaining fibers, and permits the evolution of fiber damage up to composite failure (critical crack length a_c). A Paris law links the crack growth rate (da/dN) with the ΔK_{eff}. The fatigue life is then predicted from da/dN and the computed critical size a_c.

2.4.1 Fatigue Failure Predictions

Model geometry and constitutive behavior

Under cyclic loading, the fatigue cracks in composites usually start at flaws such as interfacial reaction and broken fibers. Therefore, the simulation starts from the fiber/matrix interface at which there is an initial annular matrix crack of outer radius a_0. The initial annular crack width a_0 is taken to be the thickness of the brittle reaction layer formed during processing at the C/Ti interface of the SCS-6/Ti system, which is about 1 μm. A second initial state is considered in which the fiber inside the reaction layer crack has also failed, for which the initial crack is a penny crack of radius $R + a_0$. Probabilistic assessment of fiber fracture upon loading is used to determine which of these two initial states is relevant as a function of applied stress. We assume that the fiber/matrix (or more precisely the fiber/coating) interface is rather weak and debonds when the matrix crack impinges on the interfaces or when a fiber breaks. The interfacial shear stress τ along the debonded interface is controlled by Coulomb friction, as described in Sect. 3.2. The elastic constitutive properties of the matrix and fibers are shown in Tables 2.4 and 2.5. The elastic–plastic regime of the matrix is described by a Ramberg–Osgood relationship (2.12).

The finite element models for fatigue crack simulation are similar to those used in tensile simulation (Fig. 2.3) but an average material with composite properties is added such that the number of elements is reduced while the cracked area is kept below 1% of the model cross-section. Three FE models, each with a different matrix crack radius, were developed to predict the stress concentrations in the bridging fibers and the stress intensity factor at the crack tip, as shown in Fig. 2.14. The element sizes were selected to adequately determine the strain energy release rate along the matrix crack front, as described in "Failure simulations at fixed fatigue crack size."

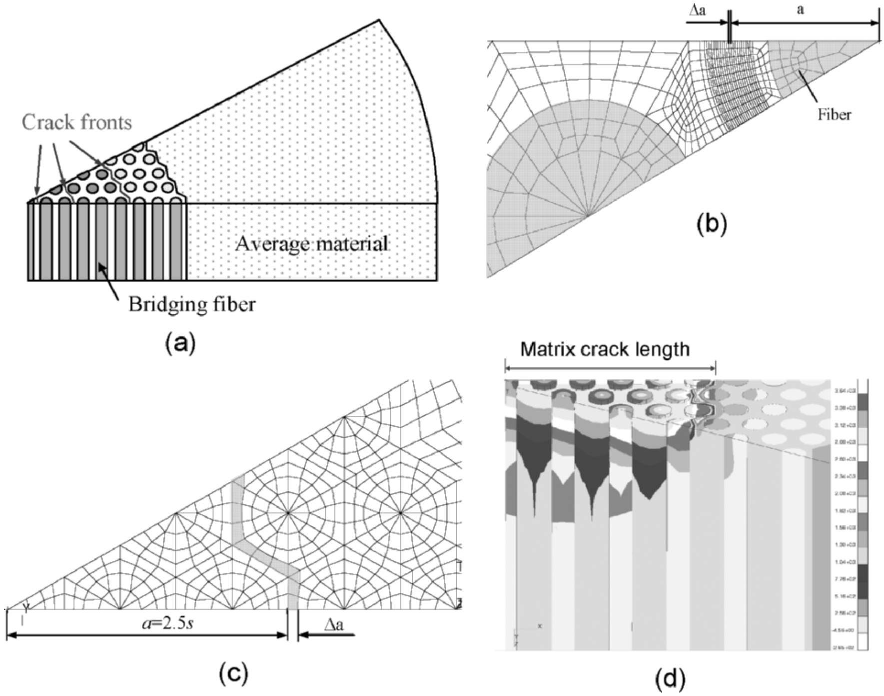

Fig. 2.14. The finite element models used here: (**a**) 30° wedge showing fibers, matrix, and average material with different crack lengths, (**b**) mesh distribution and crack tip propagation region for small matrix cracks of $a_m = 10\text{–}40$ μm, (**c**) mesh distribution and crack propagation region for an intermediate crack size of $a = 2.5s$, and (**d**) FE-predicted stress distribution in crack propagation region for a crack size of $a = 5s$ (reprinted with permission from [34])

Stress concentrations in bridging fibers

The presence of a matrix fatigue crack causes several important stress concentrations on the bridging fibers. First, there is a transfer of the matrix load onto the fibers. Second, there is an increased transfer of stress from broken fibers to unbroken fibers since the cracked matrix is not available to participate in the load sharing. Third, the matrix crack causes a stress concentration at the fiber surface that can drive "premature" fiber fracture. The calculation of the third stress concentration involves theoretical analysis and the details can be referred to in references [33, 34]. The first two factors calculated by the FE models are addressed as follows.

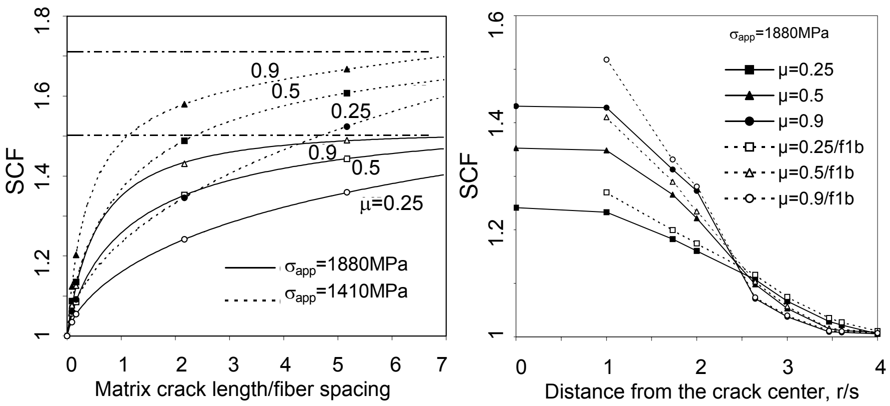

(a) **(b)**

Fig. 2.15. (**a**) Average stress concentration factor (*SCF*) on the central bridging fiber as a function of matrix crack length for applied stresses of 1,410 and 1,880 MPa. *Dashed line* shows the asymptotic SCF, (**b**) average axial SCF on the bridging fibers in and around a matrix crack of length $a = 2.5s$ (s is the fiber spacing) for an applied stress of 1,880 MPa with no broken fibers (*solid line*, *solid symbols*) and with a broken central fiber (*dashed lines*, *open symbols*) (reprinted with permission from [34])

Upon fatigue crack initiation and propagation, the fibers in the wake of the crack experience a greatly increased stress since the cracked matrix no longer carries any stress. In the limit of a large matrix crack, steady-state conditions deep within the crack dictate that the stresses on the surviving fibers in the crack plane attain the value $\sigma_f = \sigma_{comp}/V_f$. Figure 2.15a shows the average stress concentration on the central bridging fiber in the crack plane as a function of matrix crack length. For a high coefficient of friction, the maximum fiber stress becomes independent of the crack length after a relatively small amount of crack growth, i.e., steady-state conditions are reached for fairly small cracks. For a low coefficient of friction, considerable crack growth must occur before the central fiber stress becomes independent of length, i.e., steady-state conditions require rather longer crack lengths. The limiting stress concentration factor is SCF_{max} independent of the coefficient of friction.

When the central bridging fiber has failed, the stress concentrations on the surrounding surviving fibers are further elevated, as shown in Fig. 2.15b. Since the cracked matrix cannot carry any of the loads from the broken fiber, the stresses transferred to the nearby fibers are larger than those in the absence of matrix damage. Thus, the presence of the matrix fatigue crack enhances the stress on the fibers and the stress transferred from broken to unbroken fibers; both factors drive preferential damage of the fibers within the matrix crack region.

Failure simulations at fixed fatigue crack size

Fiber damage in a composite evolves stochastically due to the underlying statistical strength distribution of the brittle reinforcing fibers. Here, fiber damage in the composite is calculated using a numerical simulation technique based on the Green's function method described in Sect. 2.3. We obtain the Green's function G_{ij} in (2.5) from the full 3D finite element model, and specifically the resulting in-plane SCFs. In application to the present problem, the results of our detailed FE model with a specified matrix fatigue crack are also used to obtain the local applied field $\sigma_{\mathrm{app},i}(z)$ on every fiber in the cross-section (see Fig. 2.15, for example), which is the stress state prior to any fiber damage. Now, the effective applied stress $\sigma_{\mathrm{app},i}(z)$ in (2.6) is the stress due to applied fields plus matrix damage but not including any fiber damage.

The failure strength of composite sizes $n = 210$ and 1,024 at a gauge length of $L = 6$ mm, for various fatigue crack lengths was calculated. All calculations begin with a single initial matrix crack in the center of the composite. The calculated composite strength vs. fatigue crack size is shown in Fig. 2.16. For a fatigue crack size of zero, the simulations predict the ultimate tensile strength of the composite of about 2,300 MPa [18]. As the fatigue crack size increases, the composite strength decreases in a manner that depends strongly on the interfacial friction coefficient. For a high coefficient of friction, the higher fiber stress concentrations and surface stress concentrations drive fiber failure at smaller fatigue crack sizes. For lower coefficients of friction, the decrease in strength with increasing fatigue crack size is more gradual. The composite strength for systems with an initial fiber crack at the center of the model is also shown in Fig. 2.16. The strength of the composite is nearly independent of the existence of the initial fiber break for the lower friction coefficients. At high loads, there can be several fiber breaks, and so one additional break may not be critical. At low loads, a single fiber break cannot drive extensive additional damage; and so, again, the one break is not critical.

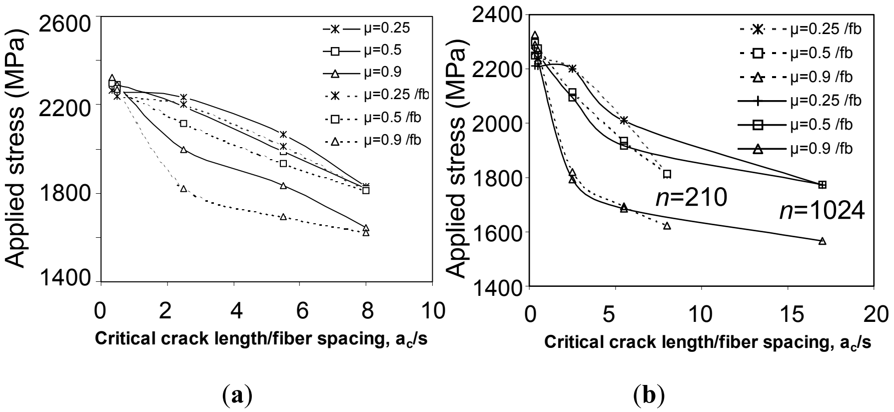

Fig. 2.16. Composite strength vs. matrix crack length for different coefficients of friction: (**a**) composite size of 210 fibers, without (*solid lines*) and with (*dashed lines*) an initial central fiber break, (**b**) composite sizes of 210 (*dashed lines*) and 1,024 (*solid lines*) with a central fiber break. As-processed fiber strength parameters are listed in Table 2.5 (reprinted with permission from [34])

2.4.2 Fatigue Life Predictions

Fatigue life predictions require the knowledge of crack growth rate as well as the initial and critical crack lengths. The critical crack length (or composite strength) has been determined in Sect. 2.4.1. To complete the computation, we must compute the number of fatigue cycles needed to reach the critical size a_c at the corresponding critical applied strength (Fig. 2.16). Here, the crack growth rate in the matrix of TMC was calculated by using fatigue properties of "neat" matrix material. Dowling and Iyyer [8] have suggested that the low-cycle fatigue crack growth rate da/dN is associated with an effective stress intensity factor range ΔK_{eff} according to a Paris law

$$\frac{\mathrm{d}a}{\mathrm{d}N} = c\Delta K_{\mathrm{eff}}^{b}, \tag{2.13}$$

where $b = 8.22$ and $c = 7 \times 10^{-16}$ m per cycle are materials constants determined via fatigue crack growth experiments on IMI834 [17]. ΔK_{eff} is related to the effective strain energy release rate range, ΔJ_{eff}, consisting of an elastic strain component ΔJ_{e} and plastic strain component ΔJ_{p}. Following Dowling and Iyyer [8], an approximation valid for an internal circular crack is used in this study to calculate the plastic term ΔJ_{p}. The term ΔJ_{e} was calculated using the FE model as follows. In linear elastic fracture mechanics, J_e equals the strain energy release rate G_I. The strain energy release rate for matrix crack growth was determined with the modified crack closure integral technique [29], given by

$$G_I = \lim_{\Delta A \to 0} \left\{ \frac{1}{\Delta A} \sum_{i=1}^{M} F_z^i u_z^i \right\}, \tag{2.14}$$

where F_z^i is the axial force on node i at the crack tip position, u_z^i is the crack tip opening of the node i after permitting the crack to grow, M is the number of crack tip nodes, and ΔA is the area of crack propagation.

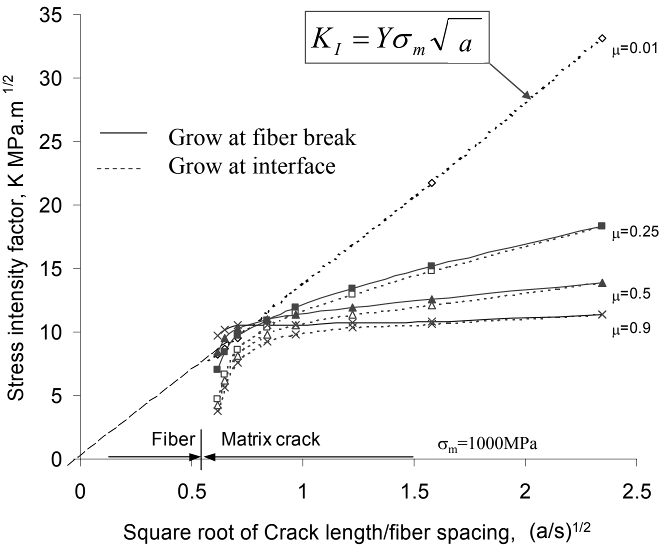

Fig. 2.17. Elastic contribution to the effective stress intensity factor K_{eff} vs. square root of the crack length a for different friction coefficients, both without (*open symbols*) and with (*solid symbols*) a central fiber break, at a matrix stress of 1,000 MPa (applied stress amplitude of 1,600 MPa, s = fiber spacing) (reprinted with permission from [34])

The elastic component of K_{eff} for a matrix stress of 1,000 MPa (corresponding to an applied stress amplitude of 1,600 MPa) is shown in Fig. 2.17 vs. crack length $a = a_m + R$, where a_m is the annular matrix crack length. The stress intensity factor for $\mu = 0.01$ follows the linear elastic fracture mechanics relation $K_I = Y\sigma_m\sqrt{\pi a}$ that is expected in the absence of fiber bridging. $Y = 0.536$ is a geometry factor whose value differs from the value $Y = 2/\pi = 0.637$ for a circular flaw in homogeneous elastic material

[33] because the higher-modulus fibers reduce the stress in the matrix. With increasing matrix crack length a ($a > 2.5s$), K_{eff} begins to approach a steady-state value independent of the crack length, and the bridging contribution to K_{eff} scales as $K_{\mathrm{b}} \propto \tau^{1/3} a^{1/2}$, similar to predictions of McCartney [21]. When the initial crack includes an in-plane fiber break, the crack growth rate is greatly accelerated in the early stages, as shown in Fig. 2.17 and as expected due to the loss of fiber bridging. For larger fatigue cracks, the crack growth rate becomes largely independent of the initial crack details; the large number of bridging fibers establishes the approach to the steady-state regime.

The calculations also show that K_{eff} increases nearly linearly before the matrix exceeds the cyclic yield point (about 850 MPa), after which K_{eff} increases more rapidly. The interfacial friction has a strong influence on K_{eff} in both elastic and plastic stages, with increased friction leading to a reduction in K_{eff} because the fiber bridging is more effective when fiber sliding is more restrained.

With the composite strength and crack growth rate as a function of fatigue crack size, as shown in Figs. 2.16 and 2.17, it is straightforward to determine the number of cycles required, at that applied stress, to grow the fatigue crack from the initial size to the final critical size. Since the initial fiber breakage does significantly reduce the fatigue life, it is important in making predictions to determine the likelihood of fiber damage upon application of the initial load. A single initial fiber break anywhere in the entire composite can serve as the site for a fast-growing fatigue crack and, hence, early fatigue failure. The probability of failure of a single fiber somewhere in a composite specimen containing n fibers with a gauge length of L is, from the Weibull statistics of fiber failure, given by

$$P_{\mathrm{f}}(\sigma_{\mathrm{comp}}) = 1 - \exp\left[\frac{Ln}{L_0} \left(\frac{\sigma_{\mathrm{comp}} - \sigma_{m\infty}(1-f)}{f\sigma_0} \right)^m \right]. \tag{2.15}$$

For small composites (e.g., $n = 210$, $L = 6$ mm), the 50% probability level for one fiber break is fairly high, at about 2,050 MPa. For a larger composite (e.g., $n = 1{,}024$, $L = 6$ mm), the 50% probability level is reduced to about 1,900 MPa. Hence, the typical stress level between having no initial fiber break and finding at least one initial fiber break is a function of composite size. To account for the possibility of initial fiber breakage, the average fatigue lifetime at any stress level should be weighted by the probability of obtaining such a fiber break. Thus, the lifetime N vs. applied stress is

$$N = N_{\mathrm{b}}(\sigma_{\mathrm{comp}})P_{\mathrm{f}}(\sigma_{\mathrm{comp}}) + N_{\mathrm{ub}}(\sigma_{\mathrm{comp}})[1 - P_{\mathrm{f}}(\sigma_{\mathrm{app}})], \tag{2.16}$$

where $N_{\mathrm{b}}(\sigma_{\mathrm{comp}})$ and $N_{\mathrm{nb}}(\sigma_{\mathrm{comp}})$ are the lifetimes for the cases of an initial fiber break and no initial fiber break at the applied stress level of interest.

The fatigue life (*S–N* curve) is calculated using the results shown in Fig. 2.18 for $N_{\mathrm{b}}(\sigma_{\mathrm{comp}})$ and $N_{\mathrm{nb}}(\sigma_{\mathrm{comp}})$, and (2.15) and (2.16) for composites with $n = 210$ and 1,024 fibers of gauge length 6 mm. The results, obtained with no adjustable parameters, are shown in Fig. 2.18 along with the experimental *S–N* data on SCS-6 fiber-reinforced IMI834 titanium alloy [32], for which the coefficient of friction is about 0.3 [16] and the sample size closely matches the simulated size. The low-cycle fatigue predictions for $\mu = 0.25$ are in very good agreement with the experimental results at stress levels higher than 1,800 MPa (lifetimes below 10^4 cycles). Below about 1,800 MPa for $\mu = 0.25$, the model predicts the aforementioned fatigue threshold whereas the actual composites continue to degrade, so that the life is overpredicted. However, the model uses only the pristine as-processed fiber strengths and explicit fatigue degradation of the fibers appears to be the cause of the reduced fatigue life for $N > 10^4$ cycles.

Guo et al. [12] found that after 10^4 cycles at a stress amplitude of 450 MPa, the extracted SiC (SCS-6) fiber surface shows a morphology similar to (uncoated) SCS-0 SiC fibers. The tensile strength of the SCS-6 fibers extracted from the fatigued specimens was reduced to a level nearly the same as that of SCS-0 fibers ($\sigma_0 = 2{,}300$ MPa, $m = 7.2$ at $L_0 = 25$ mm). Thus, it appears that low-cycle fatigue loading reduces the strength of SCS-6 fibers to that of SCS-0 fibers. We have used these fatigued fiber properties as relevant for $N > 10^4$ cycles (thereby assuming no further fatigue degradation of the fibers, consistent with the interpretation that the strength reduces only to that of the SCS-0 fibers) to calculate the composite strength vs. fatigue crack size and, subsequently, a fatigue life vs. stress. The initial fatigue crack at these low applied stresses is taken to be without a fiber break since the fibers only weaken after the $\approx 10^4$ cycles. The resulting fatigue prediction is also shown in Fig. 2.18 and contains no adjustable parameters. The predicted *S–N* curve agrees with the experimental data over the range from 1,200 to 1,500 MPa. Taken together, the two predicted results for fatigue life fall nearly along the same line, suggesting that if the fiber fatigue effect could be introduced in an appropriately gradual manner then the entire fatigue life curve would be very accurately predicted by our analysis. For the reduced fiber strengths, there is again a fatigue threshold predicted but it is at about 1,050 MPa and there is no experimental data at such low stresses. From the results shown in Fig. 2.18, interface friction is seen to play a more important, and varying, role in fatigue than in tensile strength. A higher friction coefficient is predicted to be beneficial for high-stress/low-cycle fatigue but to be detrimental at lower stresses or higher cycles.

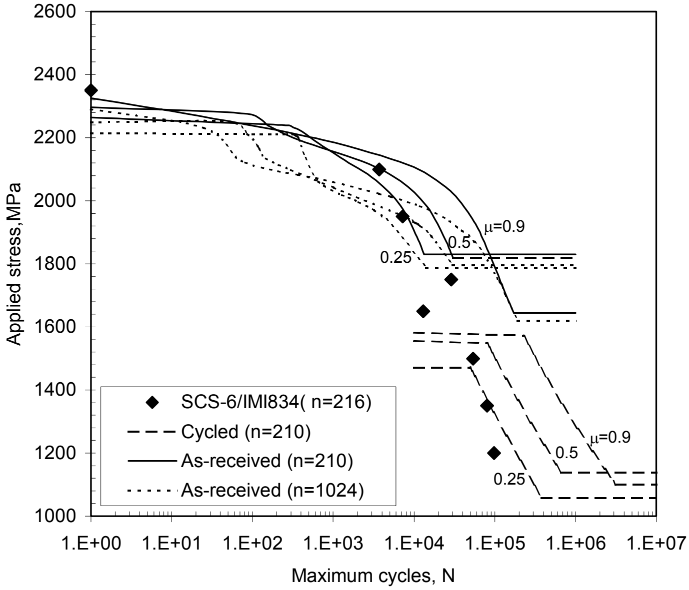

Fig. 2.18. Applied stress vs. fatigue cycles at failure (*S–N* curve, $R = 0.1$), as measured (*solid diamonds*) and as predicted (*lines*), for an SCS-6/IMI834 titanium matrix composite for different friction coefficients. Predictions use as-fabricated fiber strength (σ_0 = 4,580 MPa, L_0 = 25 mm, and m = 17) and fatigued/cycled fiber strengths (σ_0 = 2,300 MPa, L_0 = 25 mm, and m = 7.2) (reprinted with permission from [34])

2.5 Conclusions

An approach to the hierarchical modeling of composite failure has been presented. The proposed multiscale modeling involves the passing of key information from smaller to larger scales. The approach employs the FEM at the smallest scale to obtain detailed information on stress transfer from broken fibers to unbroken fibers as a function of elastic constants, fiber volume fraction, fiber/matrix interface conditions, and matrix deformation.

This detailed information is condensed into average axial SCFs on fibers around a break, which is then used as the Green's function in a larger-scale model of stochastic fiber damage evolution. In some materials, a SLM can replace the FEM/Green's function combination. Simulations of composite failure on small systems using the shear-lag or Green's function model are then performed. In the some cases, the simulated sizes can be comparable to actual test specimens so that direct comparison between model and experiment can be made; in general, this is not the case. Extensive simulations of tensile failure on small sample sizes are then used together with analytic size-scaling concepts to generate predictions for the strength vs. size and probability of failure of much larger (component size) specimens. Such large sizes could never be simulated directly, even using the highly efficient Green's function model.

Important features of the failure and deformation at each scale govern the ultimate macroscopic behavior. The interface friction coefficient and matrix-yielding behavior determine the load transfer. The shear-lag and Green's function simulations demonstrate how much damage must evolve, given the underlying load transfer, to drive tensile failure. The simulations then also provide statistical data on the size scaling. Each level of analysis is required for an accurate overall predictive methodology.

The proposed multiscale modeling approach has been used to predict the tensile strength of large-scale PMCs and MMCs. For PMCs, the predictions are in good agreement with the experimental results. In application of the method to MMCs, the success is mixed. The strength predictions for alumina fiber/Al matrix composites are comparable to the experimental values but not as accurate as SiC fiber/Ti matrix composites. The size scaling for alumina fiber/Al matrix composites is not accurately captured, with the experimental strengths decreasing faster than the predicted strengths. The absolute magnitude of the composite strength could be simply due to fiber degradation during processing, as noted above.

The present model does not consider several potential damage mechanisms that can occur in real as-fabricated coupons and components. Pre-existing fiber breaks, which can occur during processing, have not been included. Given appropriate information on the break density, however, initial breaks can easily be incorporated into the current models. Spatial irregularity of the fibers has not been included, although work by Foster [10] shows that some spatial disorder has almost no effect on the distribution of strength in a composite. The possibility of touching fibers, wherein one fiber failure immediately precipitates the second fiber failure, may be detrimental to composite strength as well and has not been addressed here. Algorithms for introducing such correlated fiber breaking are easy to generate and incorporate into the shear-lag and Green's function model.

Time- and cycle-dependent deformation and failure are both important applications issues for fiber composites. Fatigue loading induces matrix fatigue cracks, which increase the stresses on the fibers and drives damage at loads well below the quasistatic tensile strength. The multiscale modeling method has been extended to low-cycle fatigue life predictions. A finite element model is coupled with a Green's function model to simulate the major damage mechanisms occurring under fatigue loading of TMC and have predicted the low-cycle fatigue life (*S–N* curve). A finite element model containing a matrix crack bridged by SiC fibers is used to calculate both the matrix crack tip stress intensity factor and the local fiber stress concentrations due to the matrix crack as a function of the crack size. The effective crack tip stress intensity factor, including the effect of the matrix plasticity, is then used to calculate the growth rate of the bridged matrix crack. A 3D Green's function method then uses three outputs from the FE model (1) the fiber stress states due to the matrix crack, (2) the average stress transfer from a broken fiber to unbroken fibers, and (3) the surface fiber stress concentrations, to simulate the fiber damage process and composite strength at any fixed fatigue crack size. The composite strength for a given fatigue crack size together with the number of cycles required to grow the fatigue crack to the given size at an applied stress equal to this composite strength then determines the fatigue life. Detailed application of this approach to the SCS-6/IMI834 shows very good agreement with no adjustable parameters when the appropriate fiber strengths are employed (as-processed value at low cycles, fatigued value at high cycles).

Creep deformation also influences local stress states, and the present multiscale approach may be useful as a means of transferring details of time-dependent deformation at small scales into larger-scale models of fiber damage evolution in a computationally efficient manner. Direct degradation of the reinforcing fibers, via fatigue crack growth or slow crack growth, can also occur. The present models can incorporate such degradation directly at the Green's function level by introducing time- or cycle-dependent fiber strengths. In some cases, the stresses acting on growing flaws in the fibers can, however, greatly exceed the average axial fiber stresses used in the Green's function models. Thus, additional multiscale models must be used to characterize fiber strength degradation at the fiber scale due to underlying flaw growth mechanics at much smaller scales.

The present modeling and methodology set the stage for the inclusion of other damage mechanisms that may be relevant to as-processed materials or in-service application. Within the framework of the model, one could study: the effects of processing damage on damage evaluation, fatigue growth and failure, and the quasistatic and creep failure of materials with small notches. Furthermore, the current models apply not only to metallic and polymeric matrix composites, but also to ceramic matrix composites. Future work remains to attack some of these key problems and applications to other materials systems.

Acknowledgments

This work was supported by the U.S. Air Force Office of Scientific Research within the Mechanics of Multifunctional Material and Microsystems program.

References

1. Bakuckas JG, Johnson WS (1994) NASA Technical Memorandum 109135
2. Bao G, McMeeking RM (1994) Fatigue crack growth in fiber-reinforced metal–matrix composites. Acta Metall. Mater. 42:2415–2425
3. Begley MR, McMeeking RM (1995) Numerical-analysis of fiber bridging and fatigue-crack growth in metal–matrix composite materials. Mater. Sci. Eng. A 200:12–20
4. Beyerlein IJ, Phoenix SL (1996) Stress concentrations around multiple fiber breaks in an elastic matrix with local yielding or debonding using quadratic influence superposition. J. Mech. Phys. Solids 44:1997–2039
5. Connell SJ, Zok FW (1997) Measurement of the cyclic bridging law in a titanium matrix composite and its application to simulating crack growth. Acta Mater. 45:5203–5211
6. Curtin WA (1991) Theory of mechanical-properties of ceramic–matrix composites. J. Am. Ceram. Soc. 74:2837–2845
7. Curtin WA (1999) Stochastic damage evolution and failure in fiber-reinforced composites. Adv. Appl. Mech. 36:163–253
8. Dowling NE, Iyyer NS (1987) Fatigue crack growth and closure at high cyclic strains. Mater. Sci. Eng. 96:99–107
9. Ewaids HL, Wanhill RJH (1984) Fracture Mechanics. Edward Arnold and Delftse Uitgevers Maatschappij, London, p 49
10. Foster G (1997) M.S. Thesis. Virginia Polytechnic Institute and State University, Blacksburg, VA
11. Gambone ML, Wawner FE (1997) The effect of surface flaws on SiC fiber strength in an SiC/Ti-alloy composite. J. Compos. Mater. 31:1062–1079
12. Guo SQ, Kagawa Y, Tanaka Y, Masuda C (1998) Microstructure and role of outermost coating for tensile strength of SiC fiber. Acta Metall. 46:4941–4954
13. Harlow DG, Phoenix SL (1981) Probability distribution for the strength of composite materials: a convergent sequence of tight. Int. J. Fracture 17:601–629
14. Hedgepeth JM (1961) NASA Technical Report D-822

15. Hedgepeth JM, Van Dyke PJ (1967) Local stress concentrations in imperfect filamentary composite materials. J. Compos. Mater. 1:294–304
16. Hemptenmacher J, Assler H, Peters PWM, Dudek HJ (1998) Prakt Metallogr-Pr (in German) 35:295–305
17. Kordisch T, Nowack H (1988) Mat.-wiss. u. Werkstofftech (in German) 29:215–228
18. Leucht R, Dudek HJ (1994) Properties of SiC-fiber reinforced titanium-alloys processed by fiber coating and hot isostatic pressing. Mater. Sci. Eng. A 188:201–210
19. Mahesh S, Phoenix SL (2004) Lifetime distributions for unidirectional fibrous composites under creep-rupture loading. Int. J. Fracture 127:303–360; Mahesh S, Beyerlein IJ, Phoenix SL (1999) Size and heterogeneity effects on the strength of fibrous composites. Physica D 133:371–389; Mahesh S, Phoenix SL (2004) Absence of a tough–brittle transition in the statistical fracture of unidirectional composite tapes under local load sharing. Phys. Rev. E 69:026102
20. Majumdar BS, Gundel DB, Dutton RE, Warrier SG, Pagano NJ (1998) Evaluation of the tensile interface strength in brittle-matrix composite systems. J. Am. Ceram. Soc. 81:1600–1610
21. McCartney LN (1987) Mechanics of matrix cracking in brittle-matrix fiber-reinforced composites. Proc. R. Soc. Lond. A 409:329–350
22. Oden JT, Vemaganti K, Moes N (1999) Hierarchical modeling of heterogeneous solids. Comput. Meth. Appl. Mech. Eng. 172:3–25
23. Okabe T, Nishikawa M, Takeda N, Sekine H (2006) Effect of matrix hardening on the tensile strength of alumina fiber-reinforced aluminum matrix composites. Acta Mater. 54:2557–2566
24. Okabe T, Takeda N (2002) Size effect on tensile strength of unidirectional CFRP composites – experiment and simulation. Compos. Sci. Technol. 62:2053–2064
25. Okabe T, Takeda N, Kamoshida Y, Shimizu M, Curtin WA (2001) A 3D shear-lag model considering micro-damage and statistical strength prediction of unidirectional fiber-reinforced composites. Compos. Sci. Technol. 61:1773–1787
26. Phoenix SL, Raj R (1992) Scalings in fracture probabilities for a brittle matrix fiber composite. Acta Metall. Mater. 40:2813–2828
27. Raghavan P, Ghosh S (2004) Adaptive multiscale computational modeling of composite materials. Comput. Mod. Eng. Sci. 5:151–170
28. Ramamurty U, Zok FW, Leckie FA, Deve HE (1997) Strength variability in alumina fiber-reinforced aluminum matrix composites. Acta Mater. 45:4603–4613
29. Rybicki EF, Kanninen MF (1997) A finite element calculation of stress intensity factors by a modified crack closure integral. Eng. Fract. Mech. 9:931–938
30. Sastry AM, Phoenix SL (1993) Load redistribution near nonaligned fiber breaks in a 2-dimensional unidirectional composite using break-influence superposition. J. Mater. Sci. Lett. 12:1596–1599

31. Telesman J, Ghosn LJ, Kantzos P (1993) Methodology for prediction of fiber-bridging in composites. J. Compos. Technol. Res. 15:234–241
32. Warrier SG, Majumdar BS (1999) Elastic shielding during fatigue-crack growth of titanium matrix composites. Metall. Mater. Trans. A 30:277–286
33. Xia ZH, Curtin WA (2000) Tough to brittle transitions in ceramic matrix composites with increasing interfacial shear stress. Acta Mater. 48:4879–4892
34. Xia ZH, Curtin WA (2001) Life prediction of titanium MMCs under low-cycle fatigue. Acta Mater. 49:1633–1646
35. Xia ZH, Curtin WA (2001) Multiscale modeling of fracture and failure in Al/Al_2O_3 composites. Compos. Sci. Technol. 61:2247–2257
36. Xia ZH, Curtin WA (2002) Green's function vs. shear-lag models of damage failure in fiber-reinforced composites. Compos. Sci. Technol. 62:1279–1288
37. Xia ZH, Curtin WA (2002) Shear-lag vs. finite element models for stress transfer in fiber-reinforced composites. Compos. Sci. Technol. 62:1141–1149
38. Xia ZH, Curtin WA, Peters PMW (2001) Multiscale modeling of failure in metal matrix composites. Acta Mater. 49:273–287